Accepted version: Published as https://doi.org/10.1021/acs.chemmater.3c02218

Exploration, Prediction, and Experimental Verification of Structure and Optoelectronic Properties in I_2-Eu-IV-X_4 (I = Li, Cu, Ag; IV = Si, Ge, Sn; X = S, Se) Chalcogenide Semiconductors

Tianlin Wang,[†,§] Timothy M. McWhorter,[‡,§] Garrett C. McKeown Wessler,[†] Yi Yao,[†] Ruyi Song,[‡] David B. Mitzi,[*,†,‡] and Volker Blum[*,†,‡]

[†]Thomas Lord Department of Mechanical Engineering and Materials Science and [‡]Department of Chemistry, Duke University, Durham, North Carolina 27708, United States

[*]Corresponding author e-mail: david.mitzi@duke.edu, volker.blum@duke.edu

Abstract

Recently, there has been extensive research into photovoltaic, thermoelectric, and nonlinear optics applications of chalcogenide semiconductors within the large set of defect-resistant I_2-II-IV-X_4 (I = Li, Cu, Ag; II = Ba, Sr, Eu, Pb; IV = Si, Ge, Sn; X = S, Se) compounds. Five Eu-including compounds have previously been reported within this family but a comparative study of possible structures and electronic properties of all 18 Eu-based combinations is still absent. Herein, we use hybrid density functional theory to study rare-earth-including I_2-II-IV-X_4 semiconductors with Eu on the II site, in order to further understand this family and test the geometric tolerance factor (reported in our previous work) as a tool for predicting potential stable structures. We investigate how the exchange mixing parameter of the HSE06 density functional, α, affects the energetic positions of electronic levels, especially of the localized f-electron orbitals near the band edges of the extended semiconductor structures, using literature photoemission and band gap data of EuS for comparison. Lowest-energy quaternary structure candidates, energy band structures and densities of states are computationally predicted for all eighteen materials. Based on its predicted photovoltaics-relevant band gap, the previously unknown compound $Cu_2EuSnSe_4$ was selected and synthesized. The experimental structure, lattice parameters, and bandgap of $Cu_2EuSnSe_4$ are consistent with the computational predictions, confirming a 1.55 eV band gap.

Introduction

Rare-earth (RE) elements have been studied for their notable electronic, optical, magnetic, and catalytic properties, compared with other types of metal ions, for well over a century.[1-4] The RE elements include Sc, Y and 15 lanthanides (from La to Lu) with electronic configurations of $[Xe]4f^n d^{0,1}6s^2$ (n = 1–14). For example, lanthanide chalcogenides such as Er_2Se_3, Er_2Te_3, Tb_2Te_3, Dy_2Te_3, Ho_2Te_3, and Y_2Te_3 have proven to be promising thermoelectric (TE) generator candidates due to low thermal conductivities.[5] RE ions act as dopants in TE compounds such as Bi_2Te_3,[6-8] SnTe,[9] and perovskite oxides[10] to reduce the thermal conductivity, improving the power factor and the figure-of-merit. The divalent Eu^{2+}compounds EuO, EuS and EuSe were heavily studied already in the 1960s as ferromagnetic semiconductors, with cryogenic Curie temperatures of 76 K, 17 K and 4.6 K, respectively.[11-14] In luminescence applications, there are many studies of RE doping in various materials such as CaS,[15] Li_2SrSiO_4 (LSS),[16] fluoride nanophosphors,[17] $Ba_2In_2O_5$ phosphors,[18] and $K_3LuSi_2O_7$[19] to tune the emission wavelength, broadness, and intensity. In PV devices, RE ions are used as dopants for materials such as $SrAl_2O_4$,[20] $BiFeO_3$,[21, 22] perovskites like $MAPbI_3$[23] and $CsPbI_2Br$,[24] and for transport layers[25, 26] to improve power conversion efficiencies (PCE) by tuning the band gap and increasing carrier concentration. Doping of RE ions has also been shown to reduce defects and improve stability of Pb-I perovskite solar cells by introducing a RE ion "redox shuttle" in the synthesis process.[23]

Separately, chalcogenide semiconductors have already been proven as promising candidates for various applications including TE generators,[27] photoelectrochemical (PEC) cells,[28, 29] nonlinear optical (NLO) crystals[30-32] and photovoltaics (PV).[33-35] Among the most successful commercial PV materials are zincblende CdTe and chalcopyrite $Cu(In,Ga)(S,Se)_2$, each achieving high power conversion efficiencies (PCE) of over 20%.[36] However, these materials incorporate low abundance elements, Te and In. To remedy this problem,[37, 38] kesterite $Cu_2ZnSn(S,Se)_4$, which incorporates earth-abundant alternatives Zn and Sn, has received attention as a replacement. However, due to the similarity in ionic size and coordination of Cu/Zn/Sn, anti-site defects are prevalent, and the PCE of $Cu_2ZnSn(S,Se)_4$ solar cells suffers substantially.[39-44] Given these observations, there have been many recent studies that replace one or two of these elements, such as in $Cu_2BaSnS_{4-x}Se_x$ and $Ag_2BaSnSe_4$, focusing on atomic size and coordination dissimilarity as design principles to reduce the propensity for forming anti-site defects.[44-55] In the resulting, size-discriminating chalcogenides of stoichiometry I_2-II-IV-X_4 (I denotes a monovalent, II a divalent and IV a tetravalent cation and X is a chalcogen anion), anti-site defect resistance is expected by controlling the relative size of atoms on sites I, IV, and II within the lattice to limit site exchanging of ions between different coordination environments. In a previous work by our groups, the different crystal structures adopted by all known I_2-II-IV-X_4 chalcogenide semiconductor materials with I = Li, Cu, Ag; II = Ba, Sr, Eu, Pb; IV = Si, Ge, Sn; and X = S, Se were systematically categorized by two tolerance factors, i.e., two analytical

expressions based on the geometric relationship of polyhedra within the lattice.[56] Five relevant structure types emerge, labeled according to their space groups as *Ama*2, $P3_1$, $I\bar{4}2m$, $I222$ and $Ama2^{\dagger}$. The notation $Ama2^{\dagger}$ refers to the Ag_2PbGeS_4 (APGS)-type *Ama*2 structure, which is distinct from the $Cu_2SrGeSe_4$-type *Ama*2 structure.[56] The tolerance factor approach can be used to determine whether or not a particular quaternary material may be expected to adopt a particular structure. Thereby, the tolerance factor approach enables a holistic view of the I_2-II-IV-X_4 chalcogenide semiconductor family and provides direction for the synthesis of defect-resistant multinary chalcogenides.

Despite extensive study of both RE elements and chalcogenide semiconductors, the family of potential RE-containing I_2-II-IV-X_4 semiconductors has not yet been fully explored. As mentioned above, the ionic size of site II is expected to be significant for reducing the prevalence of anti-site defects. Common I and IV site cations for this family, such as Cu^+ (0.60 Å) and Sn^{4+} (0.55 Å),[57] are quite small, suggesting that larger radius II site ions (>1 Å) should be implemented in order to prevent anti-site disorder. Among the stable RE elements, Eu, Sm and Yb may occur as divalent cations and have suitable ionic radii (Eu^{2+}: 1.25 Å, Sm^{2+}: 1.27 Å, Yb^{2+}: 1.14 Å)[57] to possibly incorporate on the II site in the lattice without incurring significant anti-site defect formation. Eu^{2+} is studied in this work due to its similarity to Sr^{2+} (1.26 Å), a well-studied II-site cation within the I_2-II-IV-X_4 family.[58-61] Successfully synthesized examples of Eu-containing I_2-II-IV-X_4 compounds include the six materials Li_2EuGeS_4,[58] Li_2EuSiO_4[59] and Cu_2EuMQ_4 (M = Si, Ge, Sn; Q = S, Se),[60, 61] which adopt the $I\bar{4}2m$ (Li_2EuGeS_4), $P3_1$ (Li_2EuSiO_4, Cu_2EuGeS_4, Cu_2EuSiS_4) and *Ama*2 ($Cu_2EuGeSe_4$, Cu_2EuSnS_4) crystallographic structure types, respectively. Lack of prior research raises the question as to whether more Eu containing I_2-II-IV-X_4 compounds might exist in the size-discriminating multinary chalcogenide structure types, which particular structure they may adopt, and what their potential properties may be (e.g., nature and size of band gap and energy levels) from the viewpoint of possible semiconductor applications.

In the present work, we use hybrid density functional theory (DFT) to systematically assess the likely structures and electronic properties of 18 prospective I_2-Eu-IV-X_4 compounds, to provide understanding that may underlie potential semiconductor applications, e.g., PV. Among current first-principles computational approaches, hybrid DFT is attractive since it remains computationally feasible for complex structures while providing access to energy levels and their differences in semiconductor compounds. Specifically, we here use hybrid DFT for two distinct purposes: (1) for the prediction of ground-state total energy differences (e.g., for finding minimum-energy structures) and (2) for energy band structures. Hybrid DFT, which includes a non-local exchange energy operator, was originally devised to predict total energy-based properties. For this use, and in non-metallic structures, standard hybrid functionals are well established and generally known to provide superior accuracy compared to computationally cheaper approximations in semilocal density functional theory.[62] We thus calculate the

total energies of all eighteen considered compounds in the I_2-Eu-IV-X_4 set for the *Ama*2, $P3_1$, $I\bar{4}2m$, *I*222 and $Ama2^{\dagger}$ structure types using a standard parameterization of the HSE06 hybrid density functional[63-65] to predict the most stable structure for each compound. These results are compared to predictions generated by the tolerance factor approach as reported in previous work.[56] In contrast, energy band structures and energetic placements of different levels are technically outside the domain of DFT, since they involve excited states rather than ground state properties.[66] For density functional approximations below the level of hybrid DFT, even the prediction of the fundamental gap of a compound, which is still a total energy difference between the lowest-energy ionization potential and electron affinity, is thwarted by the so-called "delocalization error" of these functionals.[67] More adequate many-body electronic structure approaches, e.g., the *GW* approximation for quasiparticle properties, are computationally far more expensive than hybrid DFT and can present further challenges with respect to basis set convergence and convergence of reciprocal-space sums associated with long-range contributions.[68, 69] Interestingly, due to the non-local nature of the exchange operator, hybrid DFT with appropriate numerical parametrizations has long been established as an approach that can still predict approximately reasonable fundamental band gaps[64, 70-72] and other energy levels[73] in solids. Eu-containing compounds pose an additional challenge, however, since the optimum parametrization of hybrid DFT to correctly place Eu^{2+} 4*f*-orbitals (expected to form a high-spin configuration, ^{7}Eu, with one completely-filled spin channel) might differ from prior experience in systems containing only main group or simple transition metal elements. Estimating the energetic placement of the Eu^{2+} 4*f* levels is important since they could conceivably act as effective, localized hole trap states, by oxidizing Eu^{2+} to Eu^{3+}, if placed at the top of the valence band. Conversely, if states derived from other elements form the valence band maximum, a more itinerant, band-like transport behavior might result. In the main part of this work, we therefore investigate the sensitivity of hybrid DFT-derived band structures to the parameterization of the HSE06 hybrid density functional[63-65] employed here. We focus particularly on qualitative band gaps and alignments of Eu levels in the I_2-Eu-IV-X_4 compounds, especially the Eu 4*f* level position vs. the material's band edges. For validation purposes, we compare hybrid DFT results to published angle-resolved photoemission spectroscopy (ARPES) data for EuS, and further consider published energy band gaps of previously studied members of the I_2-Eu-IV-X_4 family. We then predict the electronic properties of the I_2-Eu-IV-X_4 compounds, discuss the expected accuracy of the predictions, and comment on optical properties. Finally, one promising PV-relevant compound, $Cu_2EuSnSe_4$, is synthesized and characterized to verify the accuracy of our computational approach and validity of the computational predictions.

Methods

Computational. All calculations in this work utilize FHI-aims,[74-78] a high-precision,[79, 80] all-electron code using numeric atom-centered basis functions for numerical discretization of orbitals and densities. A linear-scaling approach to evaluate hybrid density functionals is included in FHI-aims.[81, 82] The general approaches and technical choices made in the work reported here reflect the experience gained from our previous work on multinary chalcogenide semiconductors.[45, 51, 56, 83-86] According to Hund's rules, the Eu^{2+} ion has all seven 4*f*-orbitals filled with a single electron each, in a high-spin configuration. Therefore, the initial moment of Eu is set to seven to represent the net spin moment of the Eu^{2+} ion, and all simulations include spin polarization to reflect the spin of Eu^{2+}. We employed HSE06, a short-range screened hybrid exchange correlation functional, and use a screening parameter value $\omega = 0.2$ $Å^{-1}$ [63-65] for all the computations reported in this work. Consistent with our past work, we used $\alpha = 0.25$ as the exchange mixing parameter for all *total energy* computations. The arrangement of the Eu^{2+} spins was chosen to be ferromagnetic and in principle, we could have considered other arrangements as well. However, a literature report for Cu_2EuSiS_4, Cu_2EuGeS_4, and $Cu_2EuGeSe_4$ shows that all three compounds remain paramagnetic down to temperatures of only a few K,[60] consistent with negligible effective spin interactions in these systems. Additionally, we performed exploratory calculations of our own for different spin configurations for Cu_2EuGeS_4 in a hypothetical *Ama*2 structure. We found ~1 meV total energy differences and below per Eu^{2+} ion, indicating that the detailed spin arrangement of the Eu^{2+} ions should not affect the results reported in this work. Total energies of the 18 I_2-Eu-IV-X_4 compounds were calculated for each of the five structure types (identified by the space group of the structure: *Ama*2, $P3_1$, $I\bar{4}2m$, *I*222 and $Ama2^{\dagger}$) observed for the general I_2-II-IV-X_4 family.[56] For each structure, unit cell vectors and atomic coordinates were fully relaxed until all total energy gradients with respect to lattice vectors and atomic positions were smaller than 5×10^{-3} eV/Å. We first used 'light' numerical settings to identify the most stable structure type candidate for each I_2-Eu-IV-X_4 compound. Subsequently, these lowest-energy structures and those close in energy were post-relaxed with 'intermediate' numerical settings (except for Eu atoms, for which 'tight' settings were used since no specific 'intermediate' settings exist for lanthanides in FHI-aims) to generate more accurate final geometries and total energies for further analysis. The final relaxed geometries are provided in the Supporting Information (**SI**, **Geometry information**).

As noted in the introduction, for *band structures*, we validate the detailed HSE06 parameterization, especially in view of the energetic placement of the Eu 4*f* levels. Specifically, we explore the impact of different choices of the exchange mixing parameter α on the band structure calculations, investigating the most suitable choices of α that capture both the predicted energy gap and the placement of localized Eu 4*f* derived levels in relation to the less localized states derived from the other chemical elements (Li, Cu, Ag, Si, Ge, Sn, S, Se). We note that the choice of hybrid functional parameterization (e.g., α) could also have an impact on the prediction of the relative energetic stability of different structures, i.e., at the total energy

level. However, in contrast to the use of α to obtain approximate band gap estimates, the variation of energy differences of semiconductor structures with α is much more subtle and the rationale for deviating from established choices is much less clear.[62] As an example, in past work on the relative stability of the *Ama*2 and $P3_1$ structures across the alloy series $Cu_2BaGe_{1-x}Sn_xSe_4$,[86] we have found that the HSE06 hybrid functional (α = 0.25) improves an incorrect prediction of the structure hierarchy of $Cu_2BaGeSe_4$, i.e., a predicted total energy difference inconsistent with experimental observation, from 4 meV/atom (generalized-gradient PBE functional[87], i.e., α = 0) to 1 meV/atom (HSE06 hybrid functional, α = 0.25), still with an incorrect sign. This observation is consistent with the general experience[62] in chemistry that hybrid functionals tend to improve structure predictions quantitatively, but also that the detailed choice of α is not *a priori* clear. For instance, one could expect that a slightly higher α parameter would switch the total energy balance of $Cu_2BaGeSe_4$ to the experimentally observed one. However, other factors (most importantly, neglected vibrational free energy contributions) will also affect this balance in an *a priori* unknown way. We therefore remain with α = 0.25 (fixed) for total energy predictions in the present work, since this choice is well established in the literature. The favorable comparison to experimentally known Eu-based structures in the Results and Discussion section appears to vindicate this choice.

Non-self-consistent spin-orbit coupling (SOC)[78] was included in all band structure, density of states (DOS), and normal-incidence absorption coefficient calculations. Normal-incidence absorption coefficients were calculated using the random phase approximation from the HSE06+SOC electronic structure.[23] The tables and figures that summarize band structure, DOS and predicted absorption data in the main text use α = 0.375 (value selected after considering *f*-orbital positioning; see Results and Discussion section) and those for α = 0.25 and 0.3 are provided in the **SI**, unless noted otherwise. The tetrahedron integration method was used to compute densities of states (DOSs).[88] The Γ-point-centered k-point grids used for HSE06 calculations are listed in **Table S1**, along with the respective lattice parameters. Brillouin zones and k-space paths are illustrated in **Figure S1**. The electrical and optical properties were computed with the HSE06 hybrid functional and SOC, using α parameterizations of 0.375, 0.3, and 0.25 for comparison as discussed in the text. Gaussian-broadened k-space integrals based on the k-space grids in **Table S1** and with broadening width 0.1 eV were used to calculate the imaginary and real components of the dielectric function for predictions of optical absorption coefficients.

Synthetic. Polycrystalline powder samples of $Cu_2EuSnSe_4$ were synthesized using a high temperature solid-state synthetic method from precursor compounds EuSe and Cu_2SnSe_3. EuSe was prepared using a stoichiometric ratio of Eu metal (Fisher Scientific, 99.9%) and Se (Alfa Aesar, 99.999%) loaded into a flame-dried, graphitized quartz tube within a nitrogen-filled glove box. This tube was flame-sealed under vacuum and heated from 25 to 400°C over 5 hours, then from 400 to 880°C over 4 hours. This temperature

was held for 48 hours, then slowly cooled to 25°C over 14 hours. To prepare Cu_2SnSe_3, a stoichiometric ratio of CuSe (Alfa Aesar 99.5%) and SnSe (Alfa Aesar 99.999%) was ground thoroughly and pelletized, then loaded into a flame-polished quartz tube under nitrogen atmosphere. This tube was flame-sealed under vacuum and slowly heated from 25 to 900°C over 30 hours, held at 900°C for 12 hours, then slowly cooled to 25°C over 30 hours. Bulk purities of the synthesized precursor compounds (EuSe and Cu_2SnSe_3) were verified using Powder X-ray diffraction (PXRD) to ensure a stoichiometric loading in the further reactions (**Figure S2**). To prepare $Cu_2EuSnSe_4$, stoichiometric amounts of EuSe and Cu_2SnSe_3 were thoroughly ground together and pelletized, then loaded into a flame-dried quartz tube under nitrogen. This tube was then flame sealed and heated from 25 to 650°C over 12 hours, held at temperature for 136 hours, and slowly cooled to 25°C over 12 hours. The product of this reaction is a lustrous silver-grey polycrystalline pellet. This pellet was then reground, pressed, and refired at the same temperature (650°C) twice to improve the purity of the sample. To monitor potential losses during the reaction, pellet masses were recorded before and after each synthesis and refiring step. Mass loss was observed to not exceed 2%, indicating a lack of significant vapor transport or secondary reactions with the quartz surface of the ampoule.

Experimental. PXRD data were collected under ambient conditions in the 3–70° 2θ range using a PANalytical Empyrean X-ray diffractometer with Cu Kα radiation. To determine lattice constants and phase purity of powder samples, XRD patterns were fit using a Pawley fitting approach from the PANalytical HighScore Plus software package. Diffuse reflectance spectroscopy (DRS) data were collected on polycrystalline powder samples of $Cu_2EuSnSe_4$ over a range of 400-1100 nm (1.13–3.10 eV) using an Enlitech QE-R Quantum Efficiency / Reflectivity system equipped with an integrating sphere. Diffuse reflectance spectra were then converted to absorption using the Kubelka-Munk function: $F(R) = \alpha \,/\, S = (1-R)^2 \,/\, (2R)$, wherein α is the absorption coefficient, S is the scattering coefficient, and R is the reflectance.[89] Tauc plots were constructed using $[h\upsilon \cdot F(R)]^2$ (a conversion considered appropriate to determine direct band gaps, although in itself, this conversion does not indicate whether a gap is direct or indirect) and then used to estimate optical band gaps by extrapolating a linear regression approximation of the absorption onset to the background absorption of the sub-bandgap region.

Results and Discussion

Structure Prediction. As the first step of structure prediction, the total energies of all I_2-Eu-IV-X_4 (I = Li, Cu, Ag; IV = Si, Ge, Sn; X = S, Se) compounds in the *Ama*2, $P3_1$, $I\bar{4}2m$, *I*222 and $Ama2^{\dagger}$ structure types were calculated with FHI-aims 'light' settings and full relaxation of atomic positions and lattice parameters

to find the relatively stable structures for a more refined treatment. Relative energies for all structure types using 'light' settings are listed in **Table S2**. After identifying the two or, in some cases, three lowest-energy structure types for each compound, a subsequent full relaxation of all structure parameters with the more accurate 'intermediate' settings of FHI-aims was pursued for these lowest-energy structures. For each compound, the energy difference per formula unit (eight atoms) relative to the lowest-energy structure for the composition is shown in **Table 1**. As indicated in **Table 1** by a superscript 'e,' five compounds have been experimentally synthesized previously and exist in the same, lowest energy structure types as predicted by our calculations. Among the Ag-based compounds, the sulfides show an energetic preference for the *I*222 structure (structures initially placed in the $I\bar{4}2m$ structure relax directly to form *I222*), while the $Ama2^{\dagger}$ structure is predicted to be the most stable structure type for the selenides. Within the Cu-based compounds, Cu_2EuGeS_4 and Cu_2EuSiS_4 prefer $P3_1$, while the other four compounds are predicted to prefer *Ama*2. The Li-based compounds are found to be most stable in the $I\bar{4}2m$ structure type (structures initialized as *I*222 relax directly to $I\bar{4}2m$).

Table 1. Calculated total energy differences (in eV per eight-atom formula unit) of the low-energy structures of I_2-Eu-IV-X_4 (I = Li, Cu, Ag; IV = Si, Ge, Sn; X = S, Se) in different structure types (identified based on the associated space groups), using the HSE06 functional and FHI-aims' intermediate settings. The reference energy (energy zero) for each compound is the predicted lowest-energy structure, marked in bold-face font. a: the geometries relaxed into the *I*222 structure type; b: the geometries relaxed into the $I\bar{4}2m$ structure type. e: the reported structure type in which the corresponding compounds formed experimentally (see **Table 2** for references). Blank table entries: Stability ruled out using FHI-aims' light settings (see **Table S2**).

Compound	*Ama*2	$Ama2^{\dagger}$	*I*222	$I\bar{4}2m$	$P3_1$
Ag_2EuGeS_4		0.017	**0.000**	**0.000**[a]	
$Ag_2EuGeSe_4$		**0.000**	0.022	0.022[a]	
Ag_2EuSiS_4		0.023	**0.000**	**0.000**[a]	
$Ag_2EuSiSe_4$		**0.000**	0.023	0.023[a]	
Ag_2EuSnS_4		0.006	**0.000**	**0.000**[a]	
$Ag_2EuSnSe_4$	0.011	**0.000**	0.014	0.014[a]	
Cu_2EuGeS_4	0.033				**0.000**[e]
$Cu_2EuGeSe_4$	**0.000**[e]				0.083
Cu_2EuSiS_4	0.071				**0.000**[e]
$Cu_2EuSiSe_4$	**0.000**				0.038
Cu_2EuSnS_4	**0.000**[e]				0.046
$Cu_2EuSnSe_4$	**0.000**				0.162
Li_2EuGeS_4			**0.000**[b]	**0.000**[e]	
$Li_2EuGeSe_4$			**0.000**[b]	**0.000**	
Li_2EuSiS_4			**0.000**[b]	**0.000**	

$Li_2EuSiSe_4$	**0.000**[b]	**0.000**
Li_2EuSnS_4	**0.000**[b]	**0.000**
$Li_2EuSnSe_4$	**0.001**[b]	**0.000**

A few comments are in order regarding the $I\bar{4}2m$ and $I222$ structure types, which are structurally very similar, as illustrated in **Figure S3** for two exemplary compounds Li_2EuGeS_4 and Ag_2EuGeS_4. The $I\bar{4}2m$ structure is characterized by the Li atoms Li_2EuGeS_4 residing on a special site within the lattice, which can be distinguished from the general site of the Ag atoms in $I222$ compounds such as $Ag_2EuGeSe_4$. The angles between any three Li atoms in the $I\bar{4}2m$ lattice are either 90˚ or 180˚ when viewed along the principal axes. However, in the $I222$ lattice, when viewed along the *a* and *b* axes, the Ag atoms are not aligned. By analyzing the alignment of the "I" element (Ag/Li) in each of the calculated structures, it is concluded that, for Ag-based compounds, the initial $I\bar{4}2m$ structures relax to adopt the $I222$ structure type. In contrast, for the Li-based compounds, all initial $I222$ lattices relax to adopt the $I\bar{4}2m$ structure type. Indeed, no Li-based chalcogenide materials have been reported to form in the $I222$ structure type.[56]

We next compare the results of our direct, DFT-based structure predictions to the results expected from the tolerance-factor approach to predict and rationalize I_2-II-IV-X_4 compound structures, as introduced in our previous work.[56] Specifically, two geometric tolerance factors were defined, one related to I-X bond lengths between group I cations and neighboring X anions (called t_I) and another related to IV-X bond lengths between group IV cations and neighboring X anions (called t_{IV}). Both t_I and t_{IV} also include the II-X bond length (i.e., distance between group II cation and X anion) as a denominator. In Sun *et al.*,[56] we considered different approaches for selecting the bond lengths that enter t_I and t_{IV}. We found that Shannon ionic radii did not result in t_I and t_{IV} values that can cleanly separate different structure types of actual I_2-II-IV-X_4 compounds in a two-dimensional plot with t_I as the *x* axis and t_{IV} as the *y* axis, most notably due to incorrect input values for Cu-X and Ag-X bond lengths. In contrast, using tolerance factors based on averaged, experimentally obtained bond lengths of known I_2-II-IV-X_4 materials reported in the Inorganic Crystal Structure Database (ICSD)[90] resulted in a much cleaner separation of areas associated with the $Ama2$, $P31$, $I\bar{4}2m$, $I222$ and $Ama2^{\dagger}$ structure types (reported in Figures 7 and S5 of Sun *et al.*[56]). We refer to these tolerance factors as t_I^{avg} and t_{IV}^{avg}, respectively. The first two columns of **Table S3** in the **SI** list the t_I^{avg} and t_{IV}^{avg} values that are related to the 18 compounds considered in this work. Additionally, **Table S3** includes computational tolerance factors for the actual, DFT-HSE06 relaxed lowest-energy structures computed in this work, which reasonably match the experimentally inferred t_I^{avg} and t_{IV}^{avg} values.

In **Figure 1**, we show the location of each I_2-II-IV-X_4 compound (circles) reported in our past work according to the t_I^{avg} and t_{IV}^{avg} values associated with its constituent elements (see **Table S4**). Different colors distinguish different structure types, showing that the different structures assumed by these

compounds are associated with specific areas of occurrence (approximately identified by schematic shaded areas) in the tolerance factor plot. For the present work, a key point is to compare the first-principles predicted structures of as yet unknown, Eu-containing I_2-II-IV-X_4 compounds of **Table 1** to their location in the tolerance factor plots. Indeed, the points associated with Eu-containing compounds (marked by triangles of different colors in **Figure 1**) fall into the areas that pertain to the different structures, in some cases extending them. Notably, the points labeled (11), (12) and (14), which contain Ag and Se, fall into a t_1 range beyond what was previously assessed and experimental verification of their predicted $Ama2^{\dagger}$ structures would be interesting (i.e., it is not obvious that the tolerance factor approach can maintain validity for $t_1^{avg} << 1$). The Cu-based compounds, which have $t_1^{avg} < 1.03$, are found in the region that corresponds to *Ama*2 and $P3_1$. Most of the Li- and Ag-based compounds have $t_1^{avg} > 1.04$, placing them in the region of the $I\bar{4}2m$ and *I*222 structures. There are four exceptions to the latter rule, namely the $I\bar{4}2m$ data points that correspond to Li_2BaGeS_4, Li_2BaSnS_4 ($t_1^{avg} = 1.002$) and $Li_2BaGeSe_4$, $Li_2BaSnSe_4$ ($t_1^{avg} = 1.015$). However, the data set of bond lengths used to compile **Figure 1** is derived from experimental *average* bond lengths, i.e., averages taken over multiple materials for which single crystal refinements were available. These averages do not including any actual $Li_2Ba(IV)X_4$ compounds. Interestingly, the original reference that reported the four $Li_2Ba(IV)X_4$ compounds discusses experimentally determined bond lengths for Li_2BaSnS_4, namely $d_{(Li–S)} = 2.527$ Å and two values for $d_{(Ba–S)}$ (3.173 and 3.328 Å), leading to $t_1^{exp} = 1.044$.[91] If similar trends hold for the other three compounds $Li_2Ba(IV)X_4$ compounds mentioned, the area associated with $I\bar{4}2m$ should not extend left much beyond $t_1^{exp} = 1.04$. In contrast, the areas shown in **Figure 1** overlap somewhat and delineate to what degree the tolerance factors based on *a priori* available experimental average bond lengths from existing compounds can be used to give an expectation of the possible structure of an as-yet unknown compound. We further note that the mere identification of a predicted I_2-II-IV-X_4 compound structure via the tolerance factor plot is not yet proof that it can be synthesized, since the tolerance factor plot does not contain information about the relative stability of competing phase equilibria of groups of secondary compounds that could be more stable than a single I_2-II-IV-X_4 phase. Unfortunately, the way to obtain this information computationally, i.e., by combinatorially complex searches over all possible known and unknown secondary phases, would be prohibitively expensive. Nevertheless, the mutual consistency of HSE06-predicted and tolerance factor anticipated I_2-II-IV-X_4 structures, assuming that they can form, is encouraging. As noted alongside **Table 1**, at least five of the 18 compounds studied in this work are experimentally known from previous work. Additionally, we show in Section "Experimental Verification of Computational Predictions" below that at least one newly predicted compound, $Cu_2EuSnSe_4$, can be synthesized successfully. While this compound resides on the boundary of the estimated overlapping area of $I\bar{4}2m$ and *Ama*2 in **Figure 1**, it would be firmly in *Ama*2 territory but for

the Li_2BaGeS_4, Li_2BaSnS_4 and $Li_2BaGeSe_4$, $Li_2BaSnSe_4$ data points mentioned above. In fact, *Ama*2 is found both computationally and experimentally for $Cu_2EuSnSe_4$ in the present work.

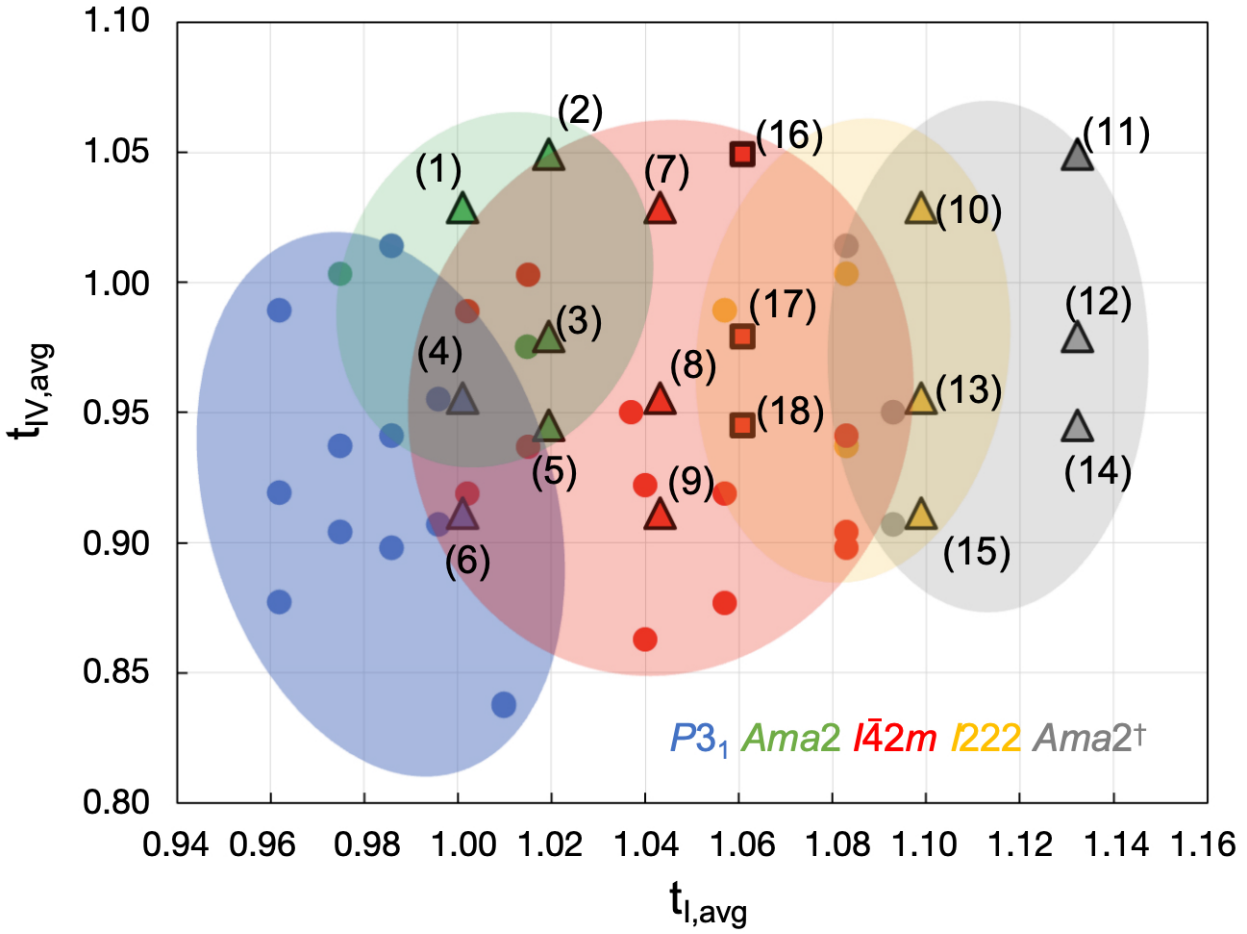

Figure 1. Tolerance factors of I_2-II-IV-X_4 compounds that have been calculated using average experimental bond lengths. The color code associated with each structure type (denoted by space group) is shown at the bottom of the figure and the overlapping shaded areas indicate the approximate areas of occurrence of each structure type. Circles: known compounds shown in **Table S4**; Triangles: compounds from this work using average experimental bond lengths to calculate tolerance factors (**Table S3**). The compounds from this work (triangles) are labelled as follows: (1) Cu_2EuSnS_4; (2) $Cu_2EuSnSe_4$; (3) $Cu_2EuGeSe_4$; (4) Cu_2EuGeS_4; (5) $Cu_2EuSiSe_4$; (6) Cu_2EuSiS_4; (7) Li_2EuSnS_4; (8) Li_2EuGeS_4; (9) Li_2EuSiS_4; (10) Ag_2EuSnS_4; (11) $Ag_2EuSnSe_4$; (12) $Ag_2EuGeSe_4$; (13) Ag_2EuGeS_4; (14) $Ag_2EuSiSe_4$; (15) Ag_2EuSiS_4; (16) $Li_2EuSnSe_4$; (17) $Li_2EuGeSe_4$; and (18) $Li_2EuSiSe_4$. Furthermore, these 18 compounds are color-coded to indicate the predicted structure type according to our calculations.

Parameter Choices of Hybrid DFT for Energy Level Predictions in Eu-containing Chalcogenides. As mentioned in the introduction, the relative alignment of energy levels near the band edges could be important, since the behavior of carriers could depend on whether the underlying states are derived from

the Eu 4*f* states or from energy levels derived from the I, IV, and X elements. We therefore assess a range of exchange mixing parameters α to gain insight into the sensitivity of predicted electronic properties to the details of the HSE06+SOC functional. For a set of benchmark semiconductors, Kim *et al.*[70] showed that the accuracy of HSE06+SOC with ω = 0.2 Å^{-1} and α = 0.25 (Krukau *et al.*'s suggestion[64]) for predictions of the fundamental band gap is of the order of several tenths of an eV. This degree of accuracy is in line with our groups' experience when comparing computed fundamental gaps to experimental band gaps for chalcogenide compounds, extracted by DRS and assuming negligible excitonic effects. For example, for Cu_2BaSnS_4, the estimated band gap from DRS is 1.95 eV[54] at room temperature, *larger* by 0.21 eV than the DFT-HSE06+SOC (ω = 0.2 Å^{-1}, α = 0.25) prediction of 1.74 eV. Note that the photoluminescence peak in Cu_2BaSnS_4 is found at 2.0 eV,[45] slightly higher than the DRS value and providing a lower bound to the experimental fundamental gap. Conversely, for the Ag-containing cubic chalcogenides $Ag_2Pb_3Si_2S_8$, $Ag_2Sr_3Sn_2S_8$, $Ag_2Sr_3Si_2S_8$, $Ag_2Sr_3Ge_2S_8$, and $Ag_2Sr_3Ge_2Se_8$, we found that experimental DRS band gap estimates are *smaller* than computationally predicted gaps from DFT-HSE06+SOC (ω = 0.2 Å^{-1}, α = 0.25) by 0.1–0.3 eV. Given this range of observations and understanding of the uncertainty involved, we have therefore employed ω = 0.2 Å^{-1} and α = 0.25 as a uniform standard for band structure computations in our past work.[45, 51, 56, 83-86]

The presence of Eu, however, adds an additional complication, since predicting the energetic placement of *f*-electron energy levels poses very different challenges[92-94] and need not follow the same empirical trends as main-group or group-11 (i.e., Cu, Ag) elements. The difficulty of predicting localized energy levels by current electronic structure methods even in seemingly standard materials is starkly illustrated in a recent benchmark paper by Piccinin[95] on the electronic structure of Fe_2O_3. In that study, different instances of the higher-level GW method arrive at energy band gap values between 1.44 eV and 5.05 eV, with values from different hybrid DFT methods ranging in between. Thus, a blackbox application of a given electronic structure method will not automatically lead to reliable predictions without careful validation and estimates of associated uncertainties. We therefore first assess the expected quality of hybrid DFT predictions for a reference system, the energy band structure of the semiconductor EuS, for which an ARPES study exists. The leftmost frame of **Figure 2** shows a reproduction of the experimental ARPES spectra of EuS[96]. The remaining frames of **Figure 2** show computed energy band structures using the spin-orbit coupled HSE06 functional for α values ranging from 0.125 to 0.5 (ω = 0.2 Å^{-1} is kept fixed for this discussion). The fundamental band gap of EuS, though an important semiconductor characteristic, cannot be inferred from ARPES spectra, which only span occupied, not unoccupied states, and we are not aware of corresponding inverse photoemission spectroscopy data that could reveal the gap. A literature search revealed that band gap estimates for EuS are largely based on optical spectroscopy, i.e., an excited state method not strictly on equal footing with ARPES. Busch, Junod and Wachter[12] first reported a room-

temperature absorption gap (paramagnetic phase, using DRS) of 1.645 eV. However, the DRS gap varies with temperature,[13] reaching a maximum of 1.69 eV at T = 36 K and falling to 1.51 eV at T = 2.4 K (ferromagnetic phase). Photoconductivity (i.e., photovoltaic) measurements show that the half maximum photoconductivity coincides with the room-temperature DRS band gap,[97] suggesting that optical excitation occurs directly into the conduction band, i.e., strong excitonic effects do not occur at room temperature. While our hybrid DFT calculations neglect any electron-hole coupling and some electron-hole coupling could still be included in the low-temperature optical data from DRS, the state of the material reflected in the calculations corresponds most closely to the ferromagnetic phase at 2.4 K and the experimental low-temperature fundamental gap of EuS is expected to be 1.51 eV or marginally higher.

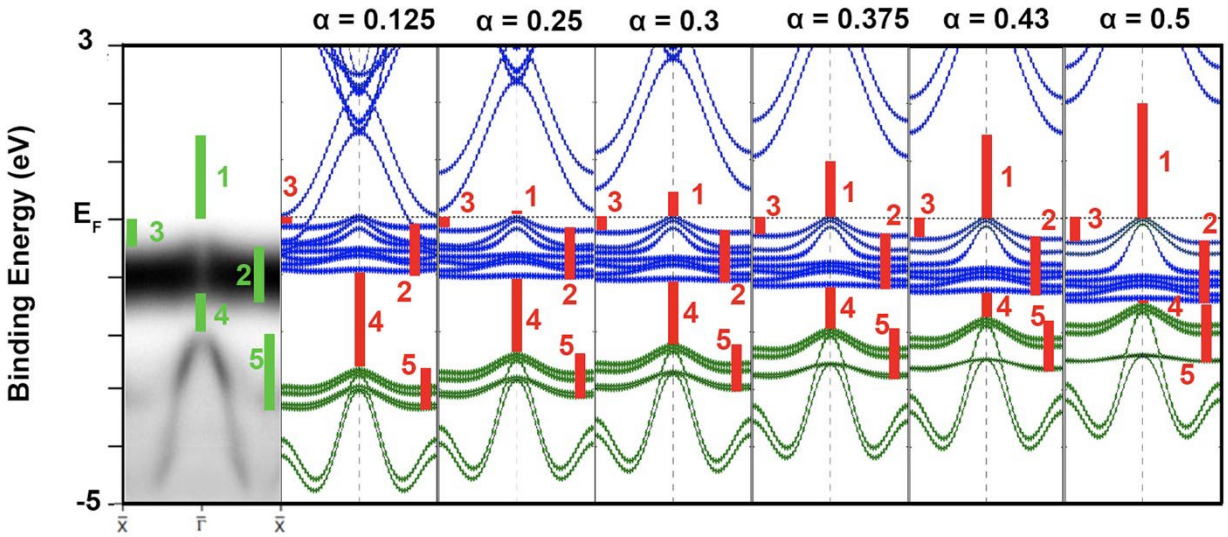

Figure 2. Leftmost frame: Experimental angle-resolved photoemission spectroscopy (ARPES) results at 20 K for EuS from the literature.[96] The experimental DRS band gap value of 1.51 eV at 2.4 K from Busch and Wachter[13] is used as the bar marked "1" in the experimental data, since an actual fundamental gap cannot be obtained from ARPES. Other frames: Calculated band structures (HSE06 functional with spin-orbit coupling) for EuS from the $\overline{X}$ to the $\overline{\Gamma}$ and then to the $\overline{X}$ position. The $\overline{X}$ point is found at (0, 1.054 Å^{-1}, 0), i.e., (0.5, 0, 0.5) in units of the primitive reciprocal lattice vectors of the rocksalt structure. Band contributions primarily associated with Eu are marked with dark blue color to distinguish them from the primarily S-derived bands (dark green color). The green and red bars with numbers mark specific band structure features used to quantitatively compare the results of various exchange parameter choices to the experimental data. Experimental data reprinted (adapted) with permission from *J. Phys. Chem. Lett.* 2021, 12, 34, 8328–8334. Copyright 2021 American Chemical Society.

The green bars and numbers superimposed on the experimental ARPES spectra in **Figure 2** indicate five specific energy differences that we use for a quantitative comparison to the calculated HSE06+SOC energy band structures of EuS. A quantitative summary of these differences is provided in **Table S5**, together with least-square prediction error averages. As can be seen from **Figure 2**, the fundamental gap (feature 1) closes for α = 0.125, i.e., the system is erroneously predicted to be metallic. The reason for this is the elevated energetic position of the seven 4*f* states filled by one electron each (spin-up) of Eu (the group

of largely flat, blue-colored bands near the Fermi energy) within the gap between the other states, i.e., non-4*f* Eu-derived and S-derived states. For the Krukau parameterization of HSE06 (α = 0.25), which we have used in the past, a very narrow energy gap (0.437 eV, feature 1) appears, but the 4*f* states are still incorrectly close to the higher-lying non-4*f* derived Eu levels. The scenario changes towards α = 0.3 and α = 0.375, which show increasing band gaps above the Eu 4*f* states (1.428 eV for α = 0.375 vs. 1.51 eV reported from low-temperature DRS). Conversely, the difference between the Eu 4*f* states and the lower-lying S-derived valence bands (feature 4) shrink as α increases and roughly coincides with the experimentally observed value (~0.7 eV) at α = 0.375. As a whole, the Eu 4*f* derived bands shift downwards between the valence and conduction bands made up of other states, reaching their approximate, experimentally observed position for α = 0.375 and higher. The approximate band width of the Eu 4*f* bands (feature 2) is also correctly captured for α = 0.375.

Table 2. DFT-HSE06+SOC predicted fundamental band gap values for several multinary compounds investigated in this work (identified by formal composition and space group), as well as experimental band gap values extracted from DRS and analysis in terms of Tauc plots in past references. Specifically, fundamental gaps were predicted for α = 0.25 and α = 0.375 (values given in black) and their gaps were categorized as direct (D), indirect (I) or quasi-direct (QD), where the latter terminology indicates a band gap that is technically indirect, but the difference to the smallest direct gap is within ~0.02eV (≈k_BT at ambient temperature). The experimental band gap values are marked with a superscript "b", taken from the references indicated in the "Reference" column. For each experimentally reported energy gap value, the hypothetical α parameter that would have predicted this gap is determined by linear interpolation / extrapolation of the α = 0.25 and α = 0.375 band gap values and is marked with a superscript "a".

Compound	Space Group	Exchange Parameter	Band Gap(eV)	Reference
Cu_2EuSiS_4	$P3_1$	0.25	2.719(I)	[60]
		0.375	3.626(D)	
		0.201[a]	2.36(D)[b]	
Cu_2EuGeS_4	$P3_1$	0.25	2.199(I)	[60]
		0.375	3.005(I)	
		0.269[a]	2.32(D)[b]	
$Cu_2EuGeSe_4$	$Ama2$	0.25	1.565(I)	[60]
		0.375	2.203(I)	
		0.284[a]	1.74(I)[b]	
Cu_2EuSnS_4	$Ama2$	0.25	1.524(QD)	[98]
		0.375	2.485(I)	
		0.299[a]	1.9[b]	
Li_2EuGeS_4	$I\bar{4}2m$	0.25	1.811(I)	[58]
		0.375	3.009(I)	
		0.313[a]	2.54(I)[b]	

Since hybrid DFT is not a true many-body theory for excited states, the α parameter that predicts the fundamental or optical band gap associated with a multinary chalcogenide compound may be different from the α parameter that correctly predicts the placement of the Eu 4*f* bands in EuS. **Table 2** shows DFT-HSE06+SOC predicted energy band gaps for several Eu containing multinary chalcogenide compounds for two different α values, α = 0.25 and α = 0.375, with experimental energy band gaps from DRS (red values) reported in the literature. As noted earlier, DRS technically does not reveal fundamental band gaps but, rather, optical band gaps, i.e., gap values that will contain the effects of some degree of electron-hole attraction and screening of a neutral excitation. Nevertheless, DRS band gaps are often the target of qualitative computational predictions and can be close to fundamental band gaps if excitonic effects are relatively small compared to the precision of an estimate by DRS, which is typically around a few hundredths of an eV depending on the precise experiment and material. For example, in the related I_2-II-IV-X_4 compounds Cu_2BaSnS_4 and $Cu_2BaGeSe_4$, the exciton binding energy contributions were found to be 25 ± 5 meV and 20 ± 5 meV, respectively, at cryogenic temperatures.[99] For the present analysis, we are interested in the α value that would have recovered the experimentally measured DRS band gap and we therefore interpolate or extrapolate to determine this value, indicated with a superscript "a" in **Table 2**. As in our own past work, we find that α = 0.25 predicts fundamental gaps that can be too low or too high by a few tenths of an eV, whereas α = 0.375 generally overestimates the DRS band gap. The estimated α values that would have reproduced the DRS band gap value exactly, assuming a linear relationship between α and the band gap, range between 0.201 and 0.313. For Cu_2BaSnS_4, a I_2-II-IV-X_4 compound from our previous work,[54, 70] the analogous "optimal" exchange parameter to match its 2.0 eV experimental band gap is α = 0.3. Taken together, the analyses of **Figure 2** and **Table 2** show that there is no single optimal α value that predicts DRS band gaps of the I_2-II-IV-X_4 chalcogenides and the location of *f* electron orbitals in Eu-containing chalcogenides. In the present work, we therefore consider several different α values, i.e., α = 0.25, α = 0.3, and α = 0.375, to provide qualitative insight into band structures and densities of states of I_2-Eu-IV-X_4 compounds.

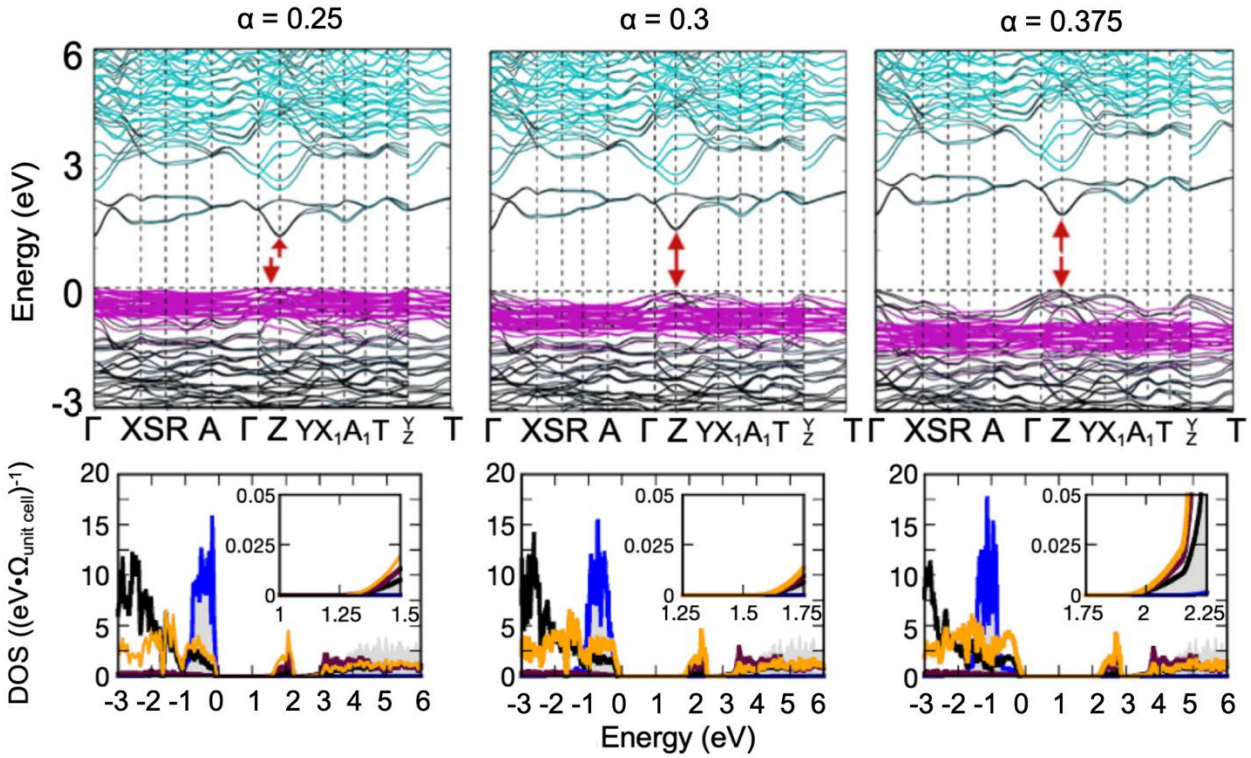

Figure 3. Upper panels: Calculated band structures and densities of states (DOSs) for $Cu_2EuSnSe_4$ in the *Ama*2 structure type, using the HSE06 functional with spin-orbit coupling and the exchange parameter (α) shown above each band structure. The positions of the valence band maximum (VBM) and conduction band minimum (CBM) are marked with red arrows. The *f* (*d*) orbital contribution from Eu is marked with magenta (cyan) color. Lower panels: Corresponding partial densities of states. The DOSs contributed by different elements are marked using the following colors: Cu: Black; Eu-total: Grey; Eu *f*-orbital: Blue; Sn: Maroon; Se: Orange. $\mathbf{\Omega}_{\text{unit cell}}$ indicates the unit cell volume.

In **Figure 3**, we illustrate the effect of α parameterization on the band structures and densities of states of $Cu_2EuSnSe_4$, the subject of our experimental investigation described later in the text. As expected from EuS, α = 0.25 places the Eu 4*f* bands (magenta) at relatively high energies, bringing them above the valence band edge defined by other elements such as Cu, Se and Sn. In contrast, the overall predicted fundamental gap of 1.28 eV is relatively low. α = 0.3 pushes the Eu bands to reside just below the valence band edge and increases the predicted bandgap to 1.53 eV**.** α = 0.375 predicts the position of the Eu bands to be more deeply within the valence band. In this case, the predicted fundamental gap is 1.88 eV. Given past experience with Cu_2BaSnS_4, the cation make-up of which differs from $Cu_2EuSnSe_4$ only by the substitution of Ba by Eu, and also the α value for Cu_2EuSnS_4 shown in **Table 2**, one might expect that $\alpha \approx 0.3$ comes close to predicting the band gap of $Cu_2EuSnSe_4$. In fact, a band gap energy of 1.55 eV is supported by our experimental assessment of $Cu_2EuSnSe_4$ below. At the same time, the discussion of EuS suggests that the α value that predicts the energetic placement of the Eu 4*f* levels should be somewhat higher than 0.3, e.g., $\alpha \approx 0.375$ as found by analyzing **Figure 2**. Based on the data in **Figure 3**, the occupied

Eu 4*f* levels would not form the valence band edges $Cu_2EuSnSe_4$ for this α range, indicating that the presence of holes might not primarily lead to Eu^{2+}/Eu^{3+} conversion and hole trapping. However, given the proximity of the energy levels in **Figure 3**, a definitive conclusion on this point is a task beyond the present work.

Electronic Band Structure Calculations: In view of the placement of the Eu 4*f* levels near the band edges, DFT-HSE06+SOC calculated band structures for $\alpha = 0.375$ are shown in **Figures 4–6** in the main text in this work, following Brillouin zone k-paths depicted in **Figure S1**. The associated band gap information is listed in **Table S6.** Analogous data for $\alpha = 0.3$ is provided in **Figures S4–S6** and **Table S7** and, for $\alpha = 0.25$, in **Figures S7–S9** and **Table S8**. The band structure comparison reveals several interesting trends. For $\alpha = 0.375$ and for the predicted stable structures, the direct and quasi-direct(a band gap that is technically indirect, but the difference to the smallest direct gap is within ~0.02eV, $\approx k_BT$ at ambient temperature) band gap values found for the Cu-based (i.e., Cu_2-Eu-IV-X_4) compounds span a wide range of 1.88–3.626 eV, while the Ag-based compounds show smaller, indirect band gaps spanning a range of values from 1.480–2.129 eV. Meanwhile, the Li-based compounds have generally larger band gaps of both indirect and direct nature, lying in a range of 2.480–3.553 eV. As expected, the calculated band gap values for $\alpha = 0.375$ are systematically larger than those calculated using $\alpha = 0.25$ and 0.3. Specifically, for $\alpha = 0.3$, the analogous band gap ranges are 1.530–3.143 eV (Cu-based), 1.191–1.782 eV (Ag-based), and 2.003–2.824 eV (Li-based), respectively. The band gap increase with α is accompanied by a shifting of the seven filled Eu^{2+} 4*f*-orbitals to lower energies with respect to the remaining valence band states. For $\alpha = 0.25$, the Eu *f* states form the top valence states for all lowest-energy predicted structures of the Cu-containing compounds (orange rims in **Figure S7**). For the Ag-derived, predicted stable structures (orange rims in **Figure S8**), the *f* orbitals appear below the highly dispersive valence band edges derived from other elements; all the Ag derived compounds are predicted to have indirect band gaps. In contrast, for $\alpha = 0.25$, the Li-containing predicted stable structures (orange rims in **Figure S9**) show the Eu *f* states located inside the band gap of the more dispersive remaining states (i.e., the non-Eu-4*f*-derived states). The energetic location of the filled 4*f* states changes systematically with increasing α, such that for $\alpha = 0.375$, the *f* orbitals for the predicted lowest-energy Cu containing compounds (orange rims in **Figure 4**) are all found below the valence band edges, again suggesting that the nature of hole quasiparticle carriers in the six Cu-containing compound semiconductors should depend sensitively on the exact balance of the key valence orbitals. In the Ag-containing compounds, the Eu *f* orbitals are simply found more deeply inside the valence bands for $\alpha = 0.375$ (orange rims in **Figure 5**)—i.e., the Ag-containing compounds are predicted to be indirect semiconductors with dispersive bands for all considered α values. A split emerges for $\alpha = 0.375$ and the Li-containing compounds (orange rims in **Figure 6**), in that the three Li_2-Eu-IV-S_4 compounds still

show the *f* orbitals forming the top of the valence bands, whereas the top of the Li_2-Eu-IV-Se_4 valence bands are narrowly predicted to be non-Eu derived. Densities of states near the band edges (in **Figures 7–9**) for α = 0.375 and in a broader energy range in **Figures S10–S12** reflect these trends as well.

It is interesting that the overall qualitative character of the band structures of the Cu-containing compounds does not change drastically if the structure type were changed to the closest-energy non-stable structures in **Table 1**. The overall band gaps would remain the same to within ~0.2 eV and, in some instances, significantly closer (**Table S6**); sometimes the *Ama2* band gap is slightly higher, sometimes slightly lower than for $P3_1$. However, if more of the Cu-derived compounds crystallized in the $P3_1$ structure type instead of *Ama2*, their band gaps would be closer to direct ones as seen in **Figure 4** for α = 0.375. For Ag-derived compounds, the scenario is different. Here, the *I*222 / $I\bar{4}2m$ structures and $Ama2^{\dagger}$ would be *energetically* close, as seen in **Table 1**, but the associated band structures change drastically in their shapes and the associated band gaps are generally higher by ~0.5–-0.6 eV in the $Ama2^{\dagger}$ structure than in *I*222. Regarding the choice of chalcogen, though the band gap values decrease when S is replaced with Se as expected, the impact of the chalcogenide anion substitution varies in different systems: in Ag-based systems, Se including compounds have band gaps that are 0.603–0.866 eV lower than their S including counterparts; in Cu-based systems, the band gap decrease is around 0.646–0.963 eV; in Li-based systems, the band gap shift is smaller, amounting to a decrease of 0.493–0.641eV.

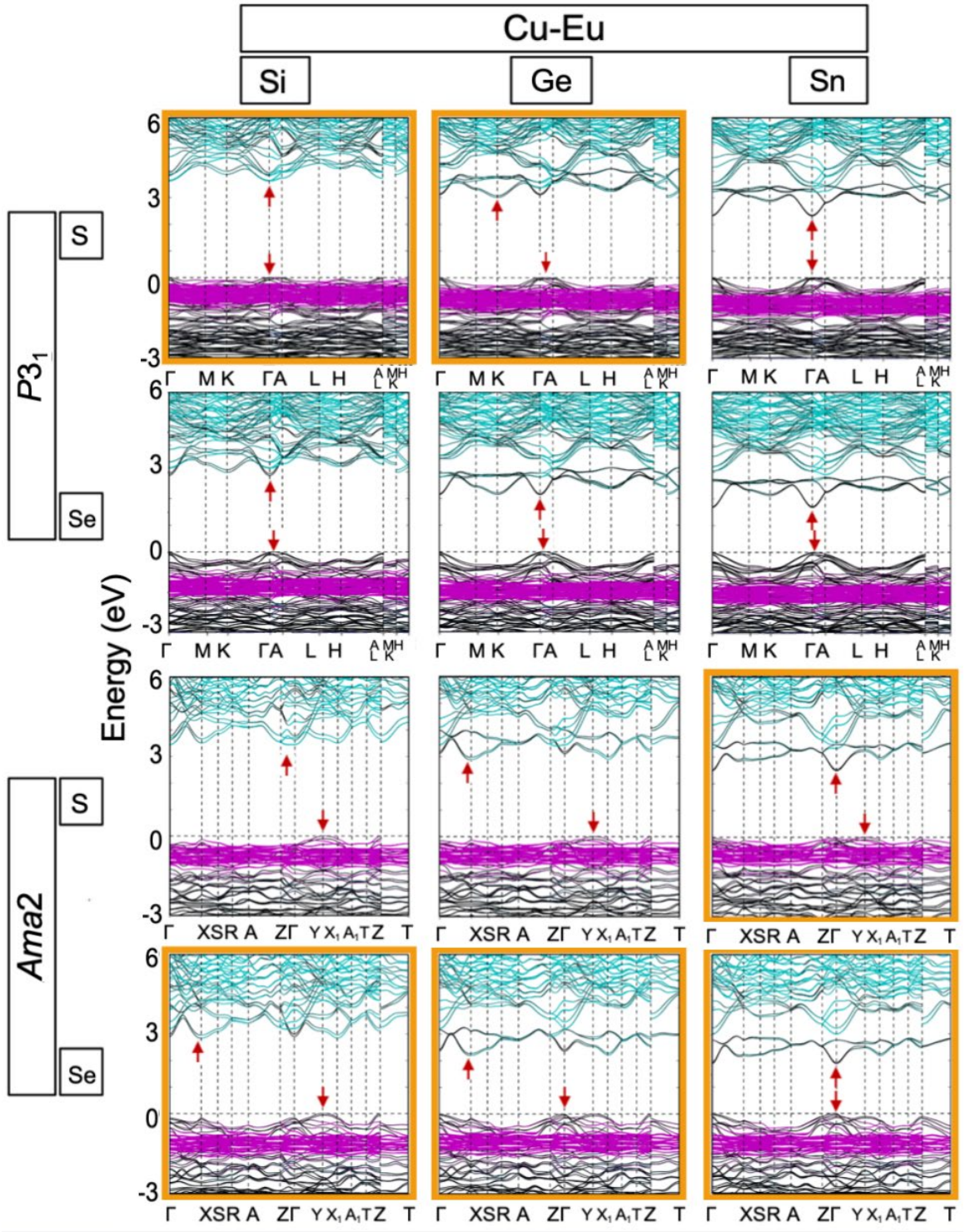

Figure 4. Calculated band structures (HSE06 functional with spin-orbit coupling using $\alpha = 0.375$) for Cu-based compounds (I = Cu; II = Eu; IV = Si, Ge, Sn; X = S, Se) as predicted in the $P3_1$ and *Ama2* structure types. In each plot, the positions of the valence band maximum (VBM) and conduction band minimum (CBM) are marked with red arrows. Orbitals to which the *f* (*d*) orbitals from Eu contribute are marked in magenta (cyan) color. The orange frames indicate the most stable structure based on the total energy computation as shown in **Table 1**.

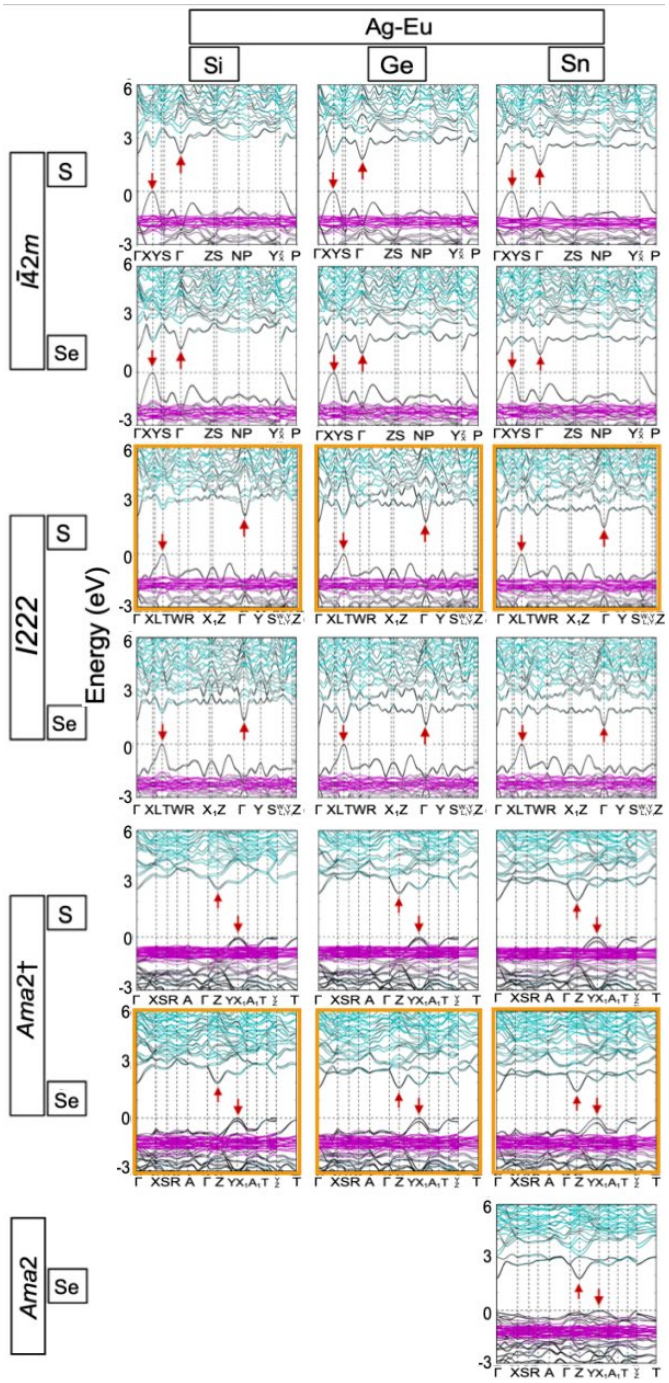

Figure 5. Calculated band structures (HSE06 functional with spin-orbit coupling using exchange parameter 0.375) for Ag-based compounds (I = Ag; II = Eu; IV = Si, Ge, Sn; X = S, Se) as predicted in the $I\bar{4}2m$, $I222$, $Ama2^{\dagger}$, and $Ama2$ structure types. The positions of the valence band maximum (VBM) and conduction band minimum (CBM) are marked with red arrows. The *f* (*d*) orbital contribution from Eu is marked with magenta (cyan) color. The orange frame indicates the most stable structure based on the total energy computation as shown in **Table 1**. Note that $I\bar{4}2m$ and $I222$ structures relax to the same structures (i.e., to the $I222$ version), but because the crystallographic unit cells have different symmetry, the selected Brillouin zone paths are chosen differently. We therefore here show band structures in both k-path conventions for better cross-comparability between compounds. $Ama2$ is energetically relatively close to the other structure types for $Ag_2EuSnSe_4$ and is therefore shown for this compound as well.

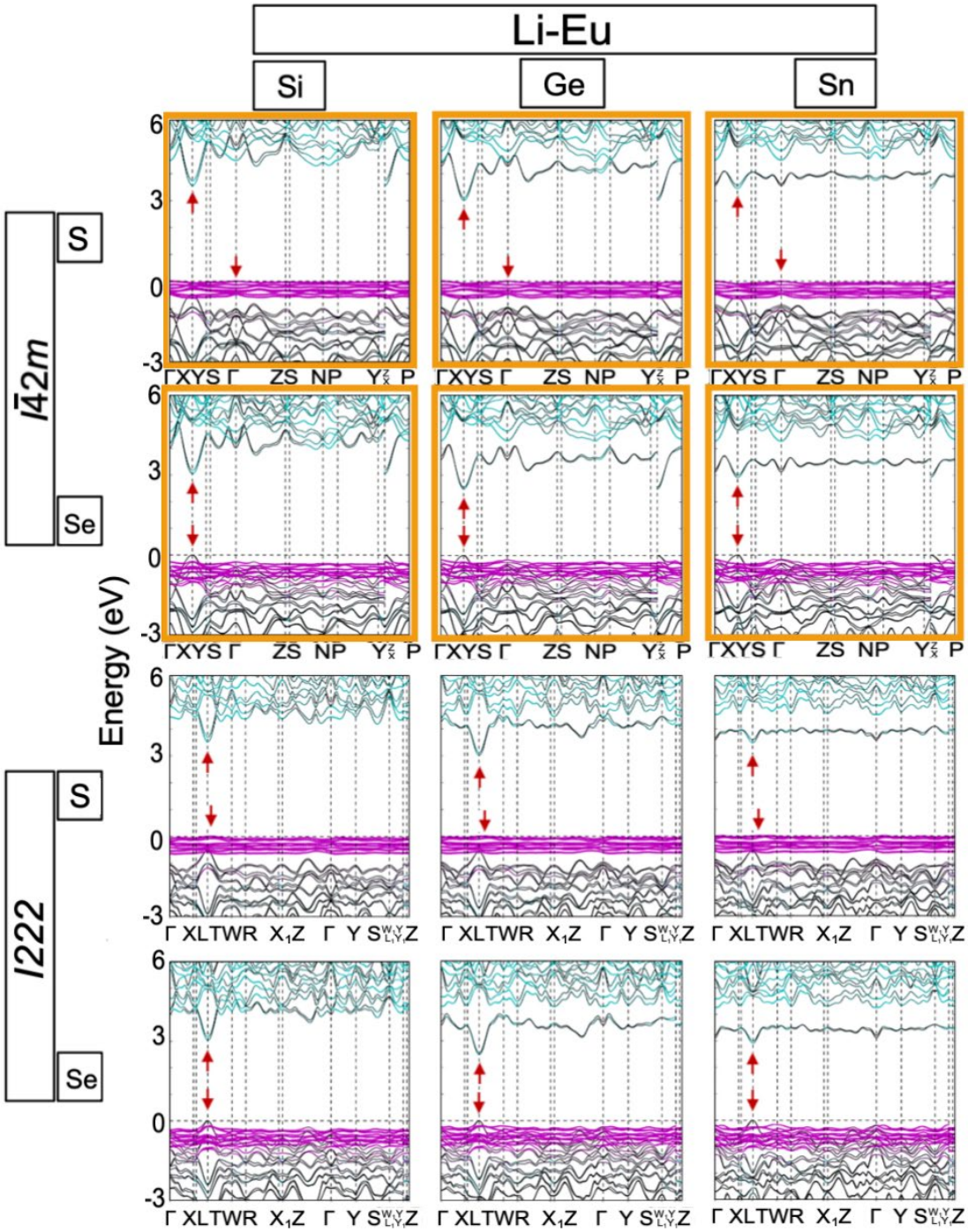

Figure 6. Calculated band structures (HSE06 functional with spin-orbit coupling using exchange parameter 0.375) for Li-based compounds (I = Li; II = Eu; IV = Si, Ge, Sn; X = S, Se) as predicted in the $I\bar{4}2m$ and *I*222 structure types. The positions of the valence band maximum (VBM) and conduction band minimum (CBM) are marked with red arrows. The *f* (*d*) orbital contribution from Eu is marked with magenta(cyan) color. The orange frame indicates the most stable structure based on the total energy computation as shown in **Table 1**. Note that $I\bar{4}2m$ and *I*222 structures relax to the same structures (i.e., to the $I\bar{4}2m$ version), but because the crystallographic unit cells have different symmetry, the selected Brillouin zone paths are chosen differently. We therefore here show band structures in both k-path conventions for better cross-comparability between compounds.

Considering the $\alpha = 0.375$ results, the Ag-based compounds show clearly indirect band gaps across all considered structure types. Therefore, these compounds are likely not ideal for absorber applications in thin-film PV devices. Although some of Cu-based compounds exhibit indirect band gaps as well, several show a direct or quasi-direct band gap. $Cu_2EuGeSe_4$ ($P3_1$), Cu_2EuSiS_4 ($P3_1$), Cu_2EuSnS_4 ($P3_1$) and $Cu_2EuSnSe_4$ (*Ama*2) all have direct band gaps and $Cu_2EuSiSe_4$ ($P3_1$) exhibits a quasi-direct gap. Our results indicate that all Li-based compounds have a direct or quasi-direct band gap, albeit with rather large band gaps in the range of 2.48–3.55 eV for $\alpha = 0.375$ (though a 1.54–2.36 eV range would result for $\alpha = 0.25$, with the localized Eu 4*f* states all forming the highest occupied states in that case, as noted above). Based on the overall trend of the band gap types and values, $Cu_2EuSnSe_4$ (*Ama*2, direct band gap: 1.88 eV as determined by $\alpha = 0.375$; 1.530 eV for $\alpha = 0.3$ and 1.284 eV for $\alpha = 0.25$) stands out as a potential candidate for PV applications. We therefore focus on the synthesis of the previously unsynthesized compound $Cu_2EuSnSe_4$ later in this work. We also note that $Ag_2EuSnSe_4$ would have a relatively favorable and nearly quasi-direct band gap if it could be stabilized in the *Ama*2 structure type (e.g., by substituting some amount of Ag with Cu) instead of the predicted $Ama2^{\dagger}$ structure type. However, at least for $\alpha = 0.375$, its predicted direct gap is practically the same as that predicted for $Cu_2EuSnSe_4$. Other materials in this family which exhibit a direct band gap show gap values which are beyond the ideal range for PV, at least for $\alpha = 0.375$.

As mentioned earlier, the observed band gap trends are also reflected in element-resolved projected densities of states near the band edges of all compounds investigated in this work. Near-band-edge DOS profiles for all the compounds are shown in **Figures 7–9**, extending from −2.0 eV to +5.0 eV (+4.0 eV for Ag-based compounds) with respect to the VBM and with the plotted DOS range limited to 1 (eV·unit cell volume)$^{-1}$ to resolve the DOS at the band edges. A broader view of the DOS appears in **Figures S10–S12**, covering the range from −3.0 eV to +6.0 eV with respect to the VBM. In Cu_2ZnSnS_4[71, 100-102] and $Ag_2ZnSn(S,Se)_4$,[103] it is known that group I and group IV metals play the dominant role in the formation of CBM and VBM, and the states from the group II element contribute little to the frontier bands. A close-up view of the DOS reveals that near the CBM, the most significant contributions are from the group X elements (S/Se) as well as the group IV (Ge/Sn) elements. However, in the Ag_2-Eu-Si-X_4 set, the contribution from Ag and X elements become the dominant species, and in Cu/Li_2-Eu-Si-X_4 set, Eu and X elements become the dominant species. Near the VBM, Eu contributes a strong peak from its 4*f*-orbitals as seen in **Figures S10–S12**. From **Figures 7–9**, the I (Cu/Ag) and X elements (S/Se) contribute significantly to the VBM as well. However, in the Li-based compounds, the contribution of Li to the VBM is minimal.

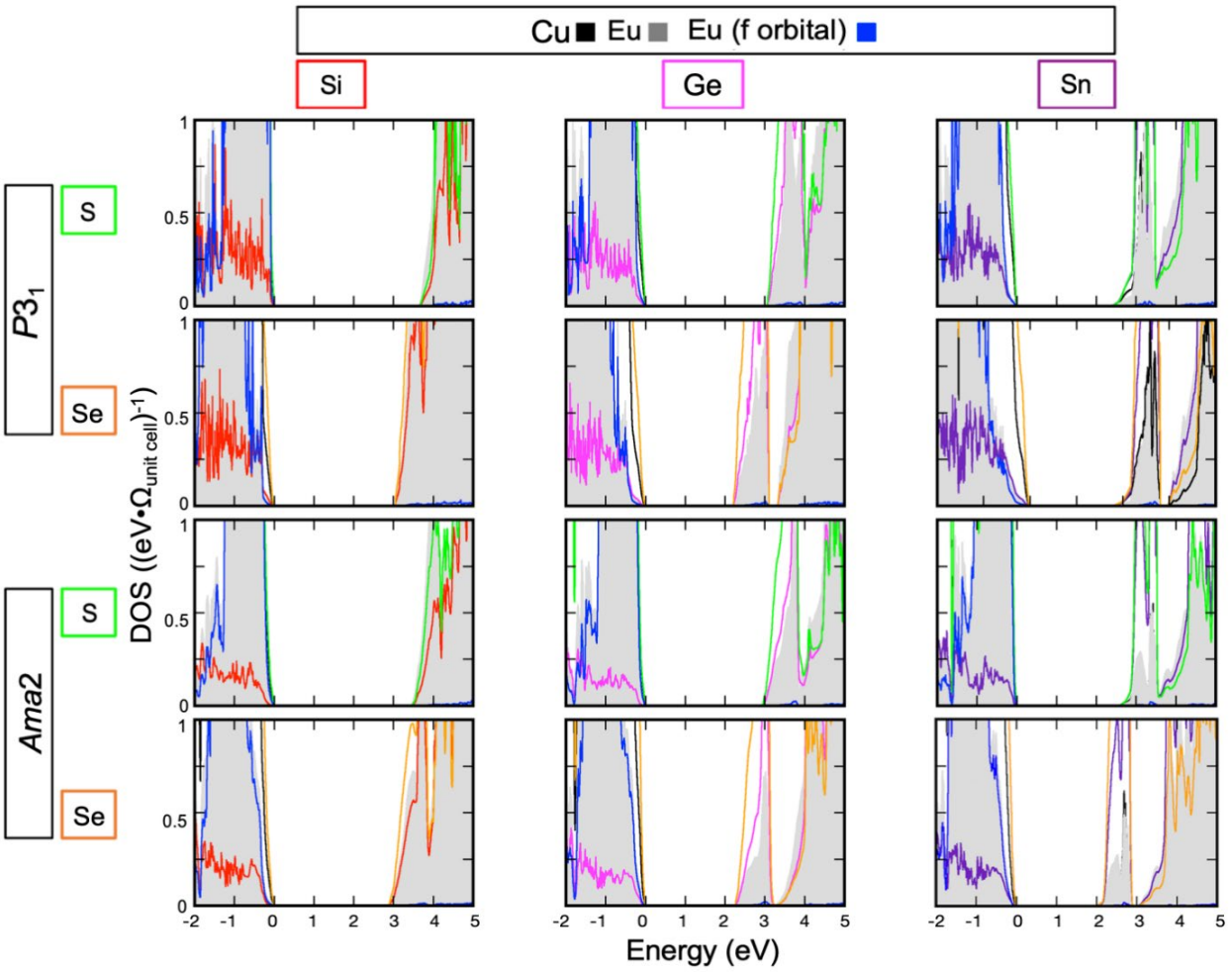

Figure 7. Calculated density of states (HSE06 functional with spin-orbit coupling and α = 0.375, using the tetrahedron integration method) for Cu-based compounds (I = Cu; II = Eu; IV = Si, Ge, Sn; X = S, Se; color scheme indicated by frames around element names in column / row headings) in the $P3_1$ and *Ama2* structure types. Regarding Eu, the shaded area reflects the total Eu contribution whereas the blue line identifies the contribution from the Eu 4*f* levels only. A more extended view of these densities of states is shown in **Figure S10**. $\mathbf{\Omega}_{\text{unit cell}}$ indicates the unit cell volume.

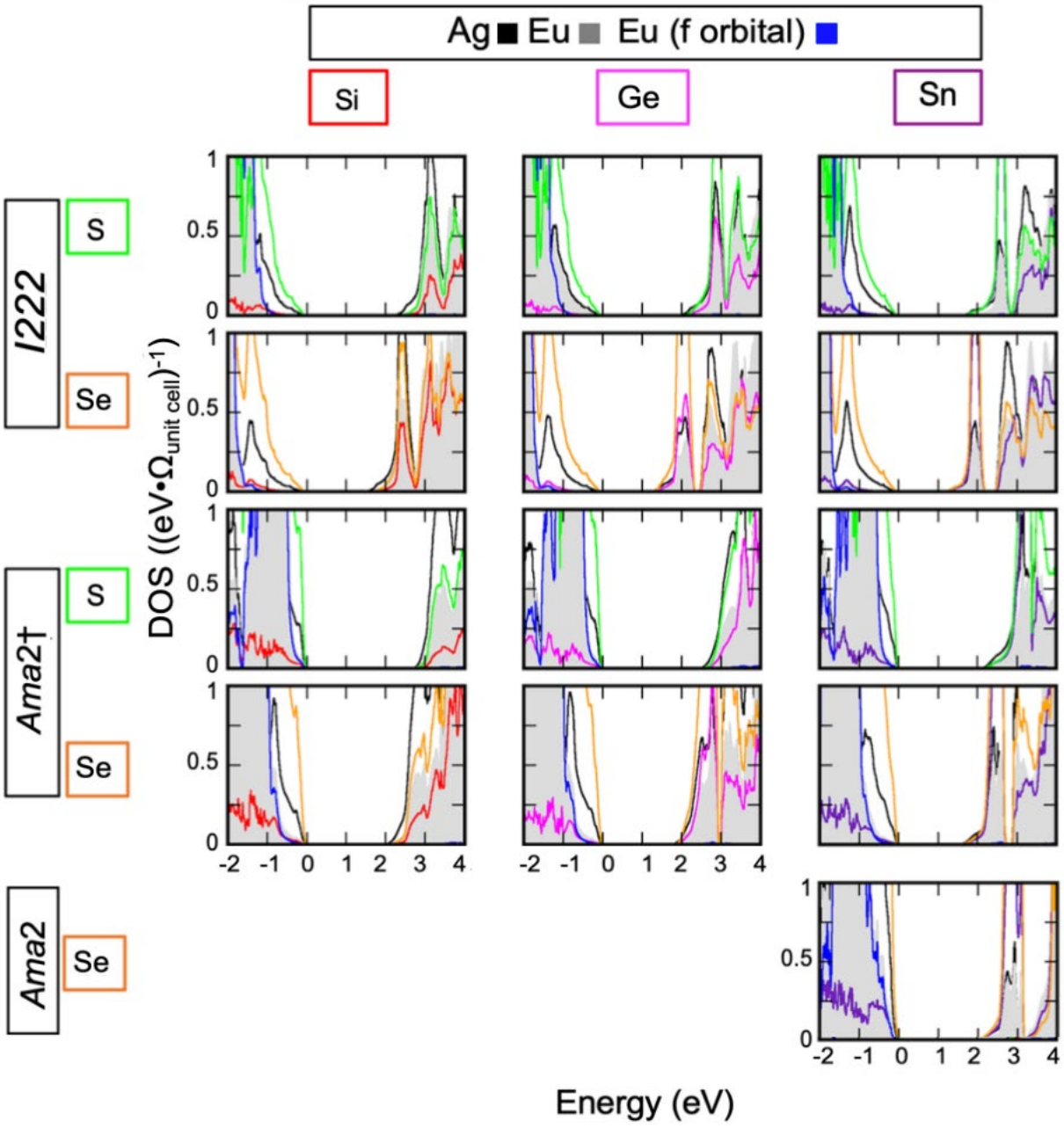

Figure 8. Calculated density of states (HSE06 functional with spin-orbit coupling and α = 0.375, using the tetrahedron integration method) for Ag-based compounds (I = Ag; II = Eu; IV = Si, Ge, Sn; X = S, Se; color scheme indicated by frames around element names in column / row headings analogous to **Figure 7**) in the *I*222, *Ama2* and $Ama2^{\dagger}$ structure types. The $I\bar{4}2m$ structure results are not shown, since using this structure type leads to relaxation into the *I*222 type. A more extended view of these densities of states is shown in **Figure S11**. $\mathbf{\Omega}_{\text{unit cell}}$ indicates the unit cell volume.

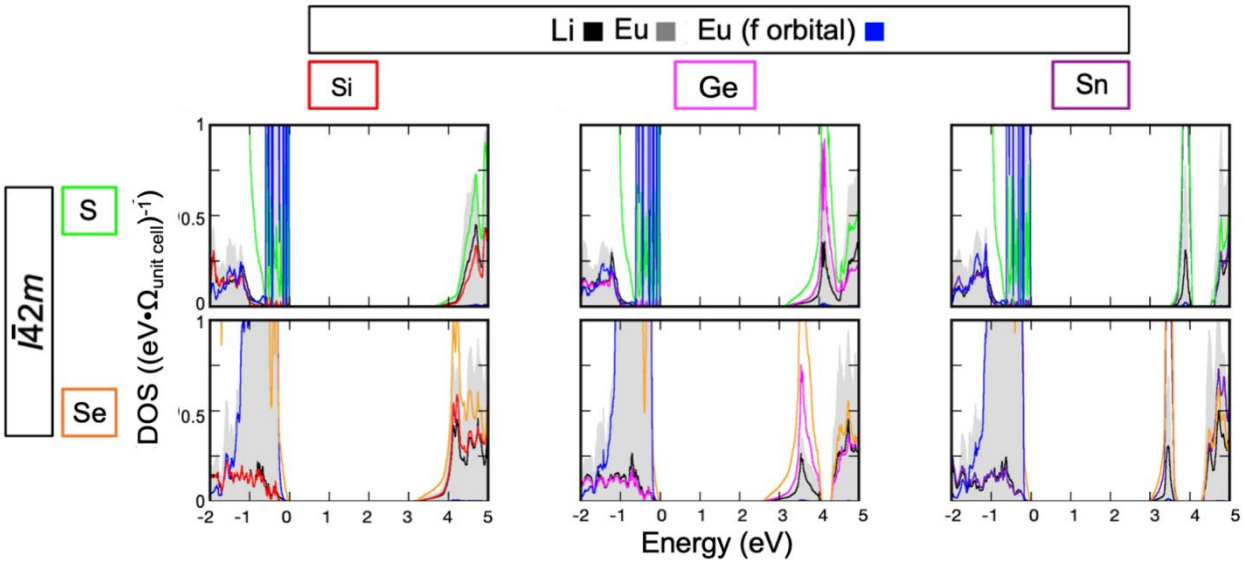

Figure 9. Calculated density of states (HSE06 functional with spin-orbit coupling and α = 0.375, using the tetrahedron integration method) for Li-based compounds (I = Li; II = Eu; IV = Si, Ge, Sn; X = S, Se; color scheme indicated by frames around element names in column / row headings analogous to **Figure 7**) in the $I\bar{4}2m$ structure type. The $I222$ structure results are not shown, since using this structure type leads to relaxation into the $I\bar{4}2m$ type. A more extended view of these densities of states is shown in **Figure S12**. **Ω**$_{\text{unit cell}}$ indicates the unit cell volume.

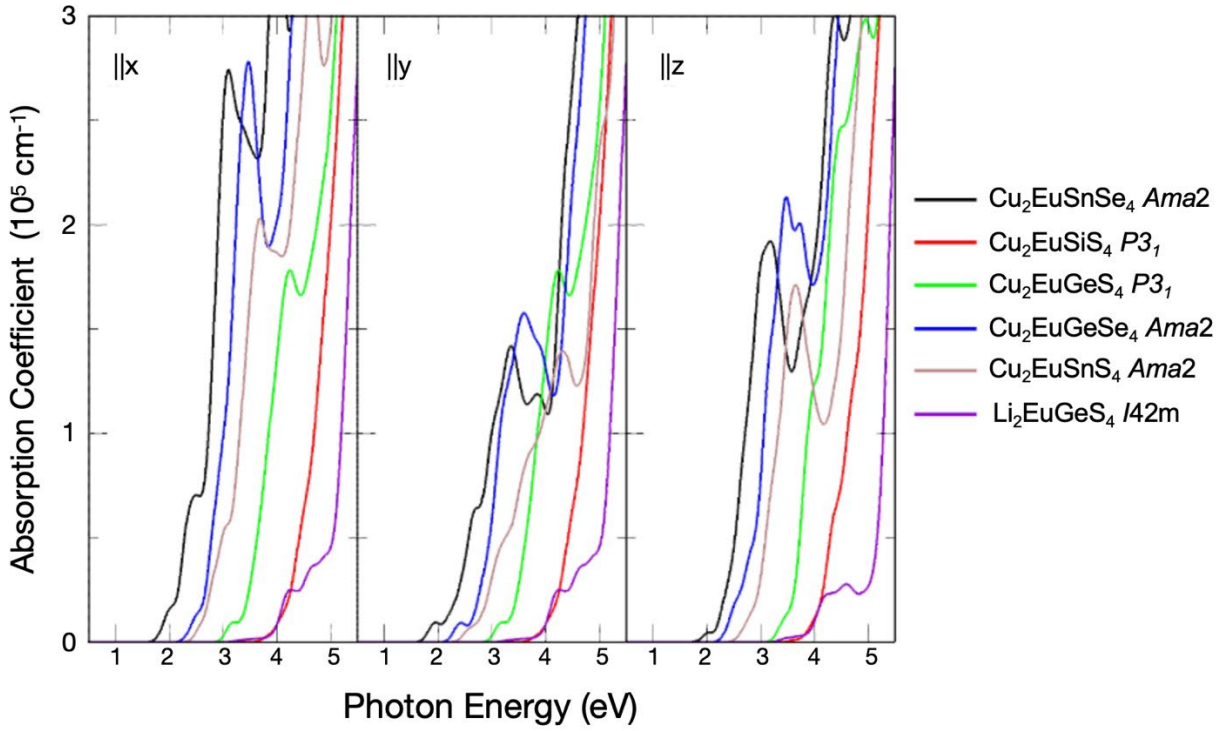

Figure 10. Anisotropic, HSE06-calculated (α = 0.375) absorption coefficients as a function of energy, parallel to different directions, where *x*, *y* and *z* reference the cartesian coordinates as used in the detailed crystal geometry files provided in the Supporting Information. A Gaussian broadening function with a width of 0.1 eV was used to produce smooth curves.

Selected Optical Property Predictions: Absorption coefficients were computed using DFT-HSE06+SOC for $Cu_2EuSnSe_4$ (*Ama*2, predicted direct band gap between 1.28 eV (α = 0.25) and 1.88 eV (α = 0.375)) and all previously synthesized compounds from **Table 2**. The calculated absorption coefficients are based on the energy bands in the independent-particle approximation and do not include any screening effects and/or attraction of electron-hole pairs. Absorption coefficients are shown in **Figure 10** for α = 0.375, within the 0.5-5.5 eV energy range to cover the visible light region (1.65–3.26 eV). Due to the anisotropy of the *Ama*2 space group, $Cu_2EuSnSe_4$ and the other Ama2 compounds display a different curve shape of absorption coefficient in all three directions. The anisotropy of absorption coefficient indicates a potential performance dependence on the crystallographic orientation for prospective thin-film solar absorbers (e.g., for PV or other optoelectronic application). However, polycrystalline films of these materials should avoid this issue unless they have a tendency for a preferred crystallization orientation with respect to the device structure. Among compounds shown in **Figure 10**, $Cu_2EuSnSe_4$ generally has the strongest optical response across the visible spectrum, with a relatively steeper predicted absorption onset than related solar absorber parent materials such as Cu_2ZnSnS_4, Cu_2BaSnS_4 or $Cu_2BaSnSe_4$.[51] Coupled with our predicted direct band gap range, this further suggests favorability of $Cu_2EuSnSe_4$ for solar absorber application.

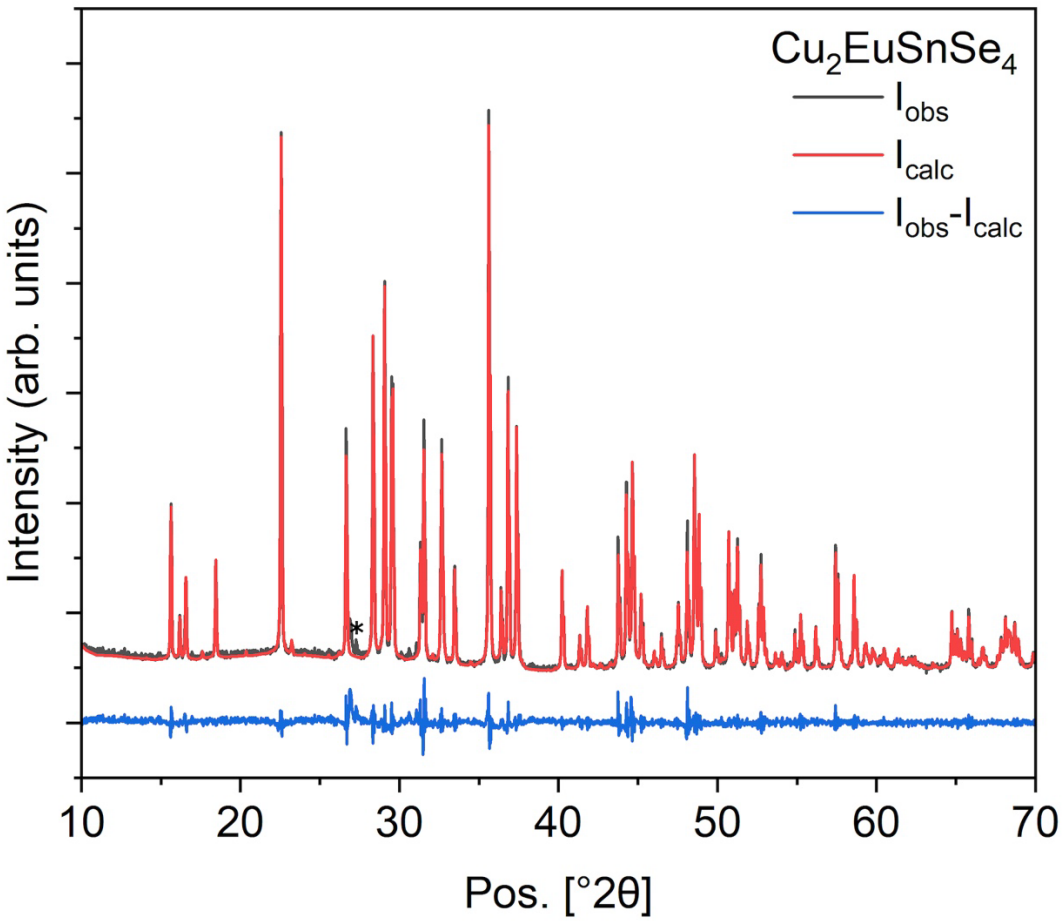

Figure 11. Powder X-ray diffraction (PXRD) spectrum collected at room temperature on a polycrystalline powder of $Cu_2EuSnSe_4$. Observed spectrum (black) is fitted against the calculated *Ama*2 spectrum (red) using a Pawley fitting, with the difference curve depicted in blue. Here, a possible trace impurity of $Cu_{1.75}Se$ has been identified and labeled with an asterisk (*).

Experimental Synthesis and Characterization of* $Cu_2EuSnSe_4$*: Following the computational analysis of this group of Eu-containing I_2-II-IV-X_4 chalcogenides, the previously unknown compound $Cu_2EuSnSe_4$ was chosen as a promising candidate for PV and other optoelectronic applications due to its predicted low and direct or quasi-direct band gap (1.28 eV−1.88 eV within the assessed range of α), strong predicted optical absorption, and similarity to previously studied PV candidate materials such as Cu_2BaSnS_4 (CBTS) and $Cu_2BaSnSe_4$ (CBTSe). This composition was targeted and synthesized for the first time using a high temperature solid state method (see Methods for details) to first determine if the predicted *Ama*2 structure is preferred over other I_2-II-IV-X_4 structures (and relative to other prospective binary, ternary and quaternary phases, which were not considered as part of the computational analysis). Polycrystalline samples of $Cu_2EuSnSe_4$ were characterized using powder X-ray diffraction (PXRD) and compared with the computationally relaxed *Ama*2 structure to verify crystal structure and bulk purity. As shown in **Figure S13,** a direct comparison of the PXRD spectrum for $Cu_2EuSnSe_4$ to a simulated diffraction pattern from

our computationally relaxed *Ama*2 structure shows good consistency. To further justify the assignment of *Ama*2 over the other possible structure types, $P3_1$, *I*222, and $Ama2^{\dagger}$ (as shown in **Table 1**), a comparison to simulated powder diffraction patterns from each relaxed structure is included in **Figure S14**. The experimentally obtained diffraction pattern is shown, and significant fingerprint regions used to differentiate *Ama*2 as our principal structural assignment are highlighted in yellow. A Pawley fitting of the PXRD spectrum is also shown in **Figure 11**. Starting from the predicted structure, Pawley fitting incorporates a refinement of predicted lattice parameters to fit the experimental spectrum (i.e., peak positions). Shown below in **Table 3**, these refined parameters are each within 1% of the predicted values as determined by computational analysis (which preceded the synthesis). Although the pattern in **Figures 11 and S13** appears to be nominally single phase, a possible trace impurity of $Cu_{1.75}Se$ is indicated with an asterisk at around 27°. Notably, we performed numerous other trial syntheses of $Cu_2EuSnSe_4$, varying reaction temperatures, starting materials (e.g., reacting pure elements Cu, Sn, Eu, and Se), reaction time, and number of annealing steps, during which we identified several other trace impurity phases that can occur during the synthesis, including the starting materials EuSe and Cu_2SnSe_3, as well as $Eu_8Sn_4Se_{20}$. The PXRD pattern in **Figure 11** reflects the empirically most successful synthesis conditions we could so far identify, as described in the experimental methods section, and serves as an existence proof of $Cu_2EuSnSe_4$, accomplishing the primary objective of this experimental investigation.

Table 3. Computationally relaxed and experimental Pawley-refined lattice parameters for $Cu_2EuSnSe_4$. A comparison between the relaxed and observed values is shown via percent difference.

	Space Group	**a (Å)**	**b (Å)**	**c (Å)**
DFT-HSE06 (α=0.25)	*Ama*2	6.747	10.791	11.028
Experimental	*Ama*2	6.690(3)	10.709(4)	10.962(4)
% Difference	-	0.84%	0.76%	0.60%

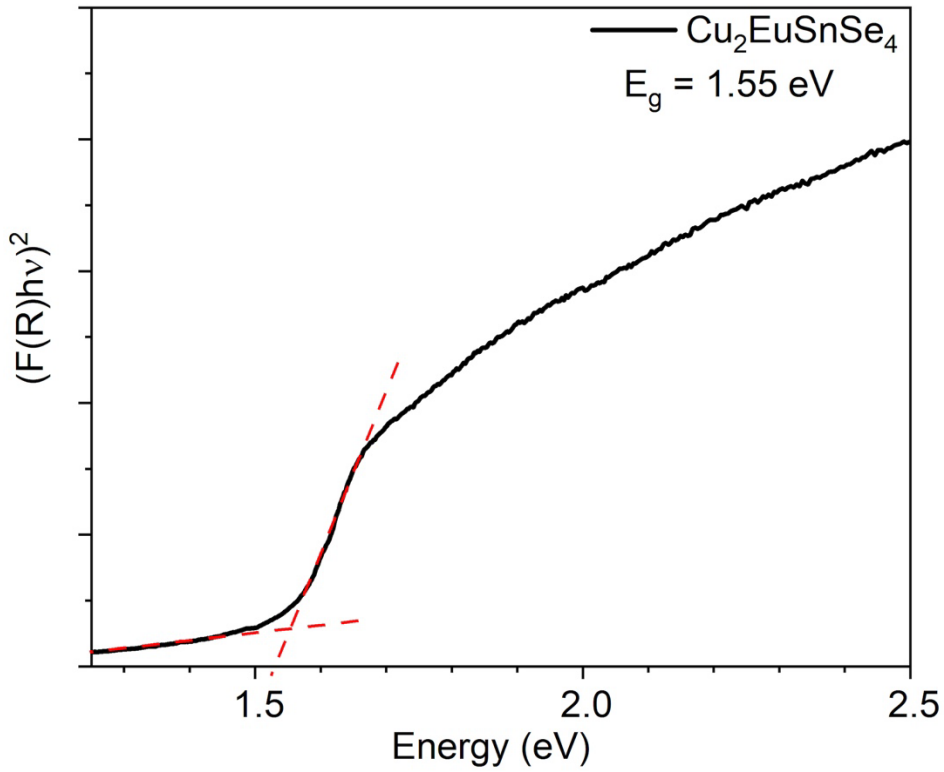

Figure 12. Direct $(F(R)\ hv)^2$ Tauc plot for $Cu_2EuSnSe_4$ powder produced from diffuse reflectance spectroscopy (DRS) data using the Kubelka Munk transform F(R). The dashed red fitting lines are used to approximate the bandgap (E_g).

To evaluate our predictions of optical properties, diffuse reflectance data for $Cu_2EuSnSe_4$ were collected and converted to absorption using the Kubelka-Munk transform (**Figure S15).** In both the absorption spectra and the associated direct Tauc plot for $Cu_2EuSnSe_4$ (**Figure 12**), we observe a sharp absorption onset. On the Tauc plot, a linear regression of this onset extrapolated to its intersection with the reflective sub-bandgap region of the spectra provides the approximate bandgap (E_g) for $Cu_2EuSnSe_4$, as indicated by the dashed red lines. Using this method, the E_g is found to be ≈1.55 eV. The DRS band gap value is lower in energy than the computationally predicted value of 1.88 eV for $\alpha = 0.375$, but is remarkably close to 1.53 eV, the prediction for $\alpha = 0.3$, the α value that would also match the DRS band gap of the known compounds Cu_2EuSnS_4 (see **Table 2**) and Cu_2BaSnS_4.[54, 70] Since $\alpha = 0.375$ was chosen to match the relative energetic positions of *f*-orbital electrons in ARPES of EuS, rather than band edges associated with Cu, Sn, and Se, it is plausible that the empirical value $\alpha = 0.3$ value, which reproduces the DRS band gap of Cu_2EuSnS_4 and Cu_2BaSnS_4, is more appropriate for describing the band gap of $Cu_2EuSnSe_4$. We also note the steep onset of the experimental absorption curve in **Figures 12 and S15**, whereas the computationally predicted onset for $\alpha = 0.375$, shown in **Figure 10** (based on the independent-

particle approximation), is substantially flatter. The *f* orbitals are also closer to the VBM for $\alpha = 0.3$ and it is conceivable that they contribute near the experimentally observed absorption onset.

Conclusions

In summary, this work presents a hybrid DFT computational analysis exploring the family of Eu-containing I_2-II-IV-X_4 (I = Li, Cu, Ag; II = Eu; IV = Si, Ge, Sn; X = S, Se) chalcogenide semiconductors and an experimental verification of our methods via the synthesis and characterization of $Cu_2EuSnSe_4$. The total energy calculations indicate that the tolerance factor approach from our previous work is a dependable tool for the approximate prediction of preferred structure type in Eu-containing I_2-II-IV-X_4 chalcogenide compounds.[56] Experimental verification through the synthesis and characterization of $Cu_2EuSnSe_4$ further supports this claim. $Cu_2EuSnSe_4$ forms in the computationally predicted *Ama2* structure type and its refined lattice parameters are within 1% of expected values from computation. To ensure a parameterization of the hybrid functional used in electronic structure determination that includes a qualitative uncertainty estimation, a range of plausible exchange mixing parameters α was evaluated through comparison with prior experimental data from the literature. The exchange mixing parameter can impact not just band gap values, but also other electronic structure features such as the location and width of specific bands. A comparison of band structure prediction and experimentally determined bandgap for $Cu_2EuSnSe_4$ vindicates this nuanced approach to α by considering a range of α values. While higher α values are needed to capture the *f* band position in literature ARPES benchmark data for EuS, a lower range of α values appears to empirically cover DRS determined band gaps in I_2-II-IV-X_4 compounds, consistent with the case of $Cu_2EuSnSe_4$. Predictions of structure and energy bands across I_2-Eu-IV-X_4 chalcogenides reveals a significant dependence on I-site composition. Our results indicate that Ag-based compounds have indirect band gaps and are most stable in the $I222$ and $Ama2^{\dagger}$ structure types. In contrast, Li-based compounds favor the $I\bar{4}2m$ structure type and have a direct gap. Though the bandgap transition in Li-based compounds is direct, the predicted E_g values are too large for most PV applications. Cu-based compounds energetically prefer the $Ama2$ and $P3_1$ structure types and contain the most promising direct bandgap materials for PV. Finally, from the band structure, DOS, and experimental results, $Cu_2EuSnSe_4$ (*Ama2*) is a promising candidate for PV and other optoelectronic application due to its direct 1.55eV band gap and strong optical response within the visible light range.

Acknowledgments

This material is based upon work supported by the U. S. Department of Energy, Office of Science, Basic Energy Sciences (BES), under contract DE-SC0020061. This work was performed in part at the Duke

University Shared Materials Instrumentation Facility (SMIF), a member of the North Carolina Research Triangle Nanotechnology Network (RTNN), which is supported by the National Science Foundation (award number ECCS-2025064) as part of the National Nanotechnology Coordinated Infrastructure (NNCI). All opinions expressed in this paper are the authors' and do not necessarily reflect the policies and views of the U.S. DOE or NSF. Computer simulations were carried out using resources of the National Energy Research Scientific Computing Center (NERSC), a U.S. Department of Energy (DOE) Office of Science User Facility operated under Contract No. DE-AC02-05CH11231.

Data Availability

The hybrid DFT calculation data for relaxation of all I_2-Eu-IV-X_4 (I = Li, Cu, Ag; IV = Si, Ge, Sn; X = S, Se) chalcogenide semiconductors and EuS, and associated energetic, electronic, and optical properties data has been deposited in the online NOMAD repository at

https://dx.doi.org/10.17172/NOMAD/2023.05.23-1

Notes

The authors declare the following competing interest(s): V.B. is a member of the executive board of MS1P e.V., the non-profit which licenses the FHI-aims electronic structure code used in this work. V.B. does not receive any financial gains from this position.

Author Contributions

[§]T.W. and T.M.M. contributed equally to this work.

Supporting Information. k-space grids and lattice parameters of each compound and structure type used in the DFT calculations. Brillouin zones and k-space paths. PXRD patterns of EuSe and Cu_2SnSe_3 precursor compounds. Calculated total energy differences for different structures of each compound. Views of the crystal structures of Li_2EuGeS_4 in the $I\bar{4}2m$ space group and of Ag_2EuGeS_4 in the *I222* space group. Tolerance factors for all compounds. Band energy differences corresponding to Figure 2. Calculated band gaps for all compounds with α=0.375. Calculated energy band structures and calculated band gaps for all compounds with α=0.3 and with α=0.25. Calculated density of states for all compounds with α=0.375.

Experimental and simulated PXRD spectra for $Cu_2EuSnSe_4$ in the *Ama2* structure. Comparison of PXRD spectra of $Cu_2EuSnSe_4$ with spectra simulated for different structure types. Absorption spectrum from diffuse reflectance data for $Cu_2EuSnSe_4$. Final computationally relaxed structures (unit cells and atomic positions) for all compounds in this work in FHI-aims geometry.in format, as well as structure used for EuS in FHI-aims geometry.in format.

Reference:

1. Chen, Y.; Liu, S.; Zhou, N.; Li, N.; Zhou, H.; Sun, L.-D.; Yan, C.-H., An overview of rare earth coupled lead halide perovskite and its application in photovoltaics and light emitting devices. *Progress in Materials Science* **2021,** *120*, 100737.
2. Urbain, G., La Phosphorescence Cathodique des Terres Rares. *Annales de Chimie et de Physique, 8th series* **1909,** *18*, 222-386.
3. Freed, S., Electronic Transitions Between an Inner Shell and the Virtual Outer Shells of the Ions of the Rare Earths in Crystals. *Physical Review* **1931,** *38* (12), 2122-2130.
4. Vleck, J. H. V., The Puzzle of Rare-earth Spectra in Solids. *The Journal of Physical Chemistry* **1937,** *41* (1), 67-80.
5. Zhu, T.; He, R.; Gong, S.; Xie, T.; Gorai, P.; Nielsch, K.; Grossman, J. C., Charting lattice thermal conductivity for inorganic crystals and discovering rare earth chalcogenides for thermoelectrics. *Energy & Environmental Science* **2021,** *14* (6), 3559-3566.
6. Ivanov, O.; Yaprintsev, M.; Lyubushkin, R.; Soklakova, O., Enhancement of thermoelectric efficiency in Bi_2Te_3 via rare earth element doping. *Scripta Materialia* **2018,** *146*, 91-94.
7. Ji, X. H.; Zhao, X. B.; Zhang, Y. H.; Lu, B. H.; Ni, H. L., Synthesis and properties of rare earth containing Bi_2Te_3 based thermoelectric alloys. *Journal of Alloys and Compounds* **2005,** *387* (1), 282-286.
8. Wu, F.; Song, H.; Jia, J.; Hu, X., Effects of Ce, Y, and Sm doping on the thermoelectric properties of Bi_2Te_3 alloy. *Progress in Natural Science: Materials International* **2013,** *23* (4), 408-412.
9. Acharya, S.; Dey, D.; Maitra, T.; Soni, A.; Taraphder, A., Rare earth doping and effective band-convergence in SnTe for improved thermoelectric performance. *Applied Physics Letters* **2018,** *113* (19), 193904
10. Sabir, B.; Murtaza, G.; Mahmood, Q.; Ahmad, R.; Bhamu, K. C., First principles investigations of electronics, magnetic, and thermoelectric properties of rare earth based $PrYO_3$(Y=Cr, V) perovskites. *Current Applied Physics* **2017,** *17* (11), 1539-1546.
11. Matthias, B. T.; Bozorth, R. M.; Van Vleck, J. H., Ferromagnetic Interaction in EuO. *Physical Review Letters* **1961,** *7* (5), 160-161.
12. Busch, G.; Junod, P.; Wachter, P., Optical absorption of ferro- and antiferromagnetic europium chalcogenides. *Physics Letters* **1964,** *12* (1), 11-12.
13. Busch, G.; Wachter, P., Einfluß der magnetischen Ordnung auf die optische Absorption von ferro- oder antiferromagnetischen Halbleitern. *Physik der kondensierten Materie* **1966,** *5* (3), 232-242.
14. Busch, G.; Junod, P.; Risi, M.; Vogt, O. In *Proceedings International Conference on Semiconductor Physics*, The Physics of semiconductors, Exeter, 16-20 July, 1962; Institute of physics and the Physical society: Exeter, 1962.
15. Joos, J. J.; Van der Heggen, D.; Martin, L. I. D. J.; Amidani, L.; Smet, P. F.; Barandiarán, Z.; Seijo, L., Broadband infrared LEDs based on europium-to-terbium charge transfer luminescence. *Nature Communications* **2020,** *11* (1), 3647.
16. Chen, J.; Guo, C.; Yang, Z.; Li, T.; Zhao, J., $Li_2SrSiO_4:Ce^{3+}$, Pr^{3+} Phosphor with Blue, Red, and Near-Infrared Emissions Used for Plant Growth LED. *Journal of the American Ceramic Society* **2016,** *99* (1), 218-225.
17. Nyk, M.; Kumar, R.; Ohulchanskyy, T. Y.; Bergey, E. J.; Prasad, P. N., High Contrast in Vitro and in Vivo Photoluminescence Bioimaging Using Near Infrared to Near Infrared Up-Conversion in Tm^{3+} and Yb^{3+} Doped Fluoride Nanophosphors. *Nano Letters* **2008,** *8* (11), 3834-3838.
18. Wang, Z.; Jiao, H.; Fu, Z., Investigating the Luminescence Behaviors and Temperature Sensing Properties of Rare-Earth-Doped $Ba_2In_2O_5$ Phosphors. *Inorganic Chemistry* **2018,** *57* (15), 8841-8849.
19. Qiao, J.; Zhou, G.; Zhou, Y.; Zhang, Q.; Xia, Z., Divalent europium-doped near-infrared-emitting phosphor for light-emitting diodes. *Nature Communications* **2019,** *10* (1), 5267.

20. Wang, L.; Guo, W.; Hao, H.; Su, Q.; Jin, S.; Li, H.; Hu, X.; Qin, L.; Gao, W.; Liu, G., Enhancing photovoltaic performance of dye-sensitized solar cells by rare-earth doped oxide of $SrAl_2O_4:Eu^{3+}$. *Materials Research Bulletin* **2016,** *76*, 459-465.
21. Biswas, P. P.; Pal, S.; Subramanian, V.; Murugavel, P., Large photovoltaic response in rare-earth doped $BiFeO_3$ polycrystalline thin films near morphotropic phase boundary composition. *Applied Physics Letters* **2019,** *114* (17), 173901.
22. Rhaman, M. M.; Matin, M. A.; Hossain, M. N.; Mozahid, F. A.; Hakim, M. A.; Rizvi, M. H.; Islam, M. F., Bandgap Tuning of Sm and Co Co-doped BFO Nanoparticles for Photovoltaic Application. *Journal of Electronic Materials* **2018,** *47* (12), 6954-6958.
23. Wang, L.; Zhou, H.; Hu, J.; Huang, B.; Sun, M.; Dong, B.; Zheng, G.; Huang, Y.; Chen, Y.; Li, L.; Xu, Z.; Li, N.; Liu, Z.; Chen, Q.; Sun, L.-D.; Yan, C.-H., A Eu^{3+}-Eu^{2+} ion redox shuttle imparts operational durability to Pb-I perovskite solar cells. *Science* **2019,** *363* (6424), 265-270.
24. Xiang, W.; Wang, Z.; Kubicki, D. J.; Tress, W.; Luo, J.; Prochowicz, D.; Akin, S.; Emsley, L.; Zhou, J.; Dietler, G.; Grätzel, M.; Hagfeldt, A., Europium-Doped $CsPbI_2Br$ for Stable and Highly Efficient Inorganic Perovskite Solar Cells. *Joule* **2019,** *3* (1), 205-214.
25. Xu, Z.; Wu, J.; Wu, T.; Bao, Q.; He, X.; Lan, Z.; Lin, J.; Huang, M.; Huang, Y.; Fan, L., Tuning the Fermi Level of TiO_2 Electron Transport Layer through Europium Doping for Highly Efficient Perovskite Solar Cells. *Energy Technology* **2017,** *5* (10), 1820-1826.
26. Hu, Z.; Chen, D.; Yang, P.; Yang, L.; Qin, L.; Huang, Y.; Zhao, X., Sol-gel-processed yttrium-doped NiO as hole transport layer in inverted perovskite solar cells for enhanced performance. *Applied Surface Science* **2018,** *441*, 258-264.
27. Shi, Y.; Sturm, C.; Kleinke, H., Chalcogenides as thermoelectric materials. *Journal of Solid State Chemistry* **2019,** *270*, 273-279.
28. Woods-Robinson, R.; Han, Y.; Zhang, H.; Ablekim, T.; Khan, I.; Persson, K. A.; Zakutayev, A., Wide Band Gap Chalcogenide Semiconductors. *Chemical Reviews* **2020,** *120* (9), 4007-4055.
29. Chen, M.-M.; Xue, H.-G.; Guo, S.-P., Multinary metal chalcogenides with tetrahedral structures for second-order nonlinear optical, photocatalytic, and photovoltaic applications. *Coordination Chemistry Reviews* **2018,** *368*, 115-133.
30. Lin, H.; Wei, W.-B.; Chen, H.; Wu, X.-T.; Zhu, Q.-L., Rational design of infrared nonlinear optical chalcogenides by chemical substitution. *Coordination Chemistry Reviews* **2020,** *406*, 213150.
31. Wu, K.; Pan, S., A review on structure-performance relationship toward the optimal design of infrared nonlinear optical materials with balanced performances. *Coordination Chemistry Reviews* **2018,** *377*, 191-208.
32. Guo, S.-P.; Chi, Y.; Guo, G.-C., Recent achievements on middle and far-infrared second-order nonlinear optical materials. *Coordination Chemistry Reviews* **2017,** *335*, 44-57.
33. Zakutayev, A., Brief review of emerging photovoltaic absorbers. *Current Opinion in Green and Sustainable Chemistry* **2017,** *4*, 8-15.
34. Le Donne, A.; Trifiletti, V.; Binetti, S., New Earth-Abundant Thin Film Solar Cells Based on Chalcogenides. *Front Chem* **2019,** *7*, 297.
35. Mitzi, D. B.; Kim, Y., Spiers Memorial Lecture: Next generation chalcogenide-based absorbers for thin-film solar cells. *Faraday Discussions* **2022,** *239* (0), 9-37.
36. Green, M. A.; Hishikawa, Y.; Dunlop, E. D.; Levi, D. H.; Hohl-Ebinger, J.; Yoshita, M.; Ho-Baillie, A. W. Y., Solar cell efficiency tables (Version 53). *Progress in Photovoltaics: Research and Applications* **2019,** *27* (1), 3-12.
37. Feltrin, A.; Freundlich, A., Material considerations for terawatt level deployment of photovoltaics. *Renewable Energy* **2008,** *33* (2), 180-185.
38. Tao, C. S.; Jiang, J.; Tao, M., Natural resource limitations to terawatt-scale solar cells. *Solar Energy Materials and Solar Cells* **2011,** *95* (12), 3176-3180.
39. Wang, W.; Winkler, M. T.; Gunawan, O.; Gokmen, T.; Todorov, T. K.; Zhu, Y.; Mitzi, D. B., Device Characteristics of CZTSSe Thin-Film Solar Cells with 12.6% Efficiency. *Advanced Energy Materials* **2014,** *4* (7), 1301465.

40. Gokmen, T.; Gunawan, O.; Todorov, T. K.; Mitzi, D. B., Band tailing and efficiency limitation in kesterite solar cells. *Applied Physics Letters* **2013,** *103* (10), 103506.
41. Rey, G.; Larramona, G.; Bourdais, S.; Choné, C.; Delatouche, B.; Jacob, A.; Dennler, G.; Siebentritt, S., On the origin of band-tails in kesterite. *Solar Energy Materials and Solar Cells* **2018,** *179*, 142-151.
42. Nishiwaki, M.; Nagaya, K.; Kato, M.; Fujimoto, S.; Tampo, H.; Miyadera, T.; Chikamatsu, M.; Shibata, H.; Fujiwara, H., Tail state formation in solar cell materials: First principles analyses of zincblende, chalcopyrite, kesterite, and hybrid perovskite crystals. *Physical Review Materials* **2018,** *2* (8), 085404.
43. Levcenko, S.; Just, J.; Redinger, A.; Larramona, G.; Bourdais, S.; Dennler, G.; Jacob, A.; Unold, T., Deep Defects in $Cu_2ZnSn(S,Se)_4$ Solar Cells with Varying Se Content. *Physical Review Applied* **2016,** *5* (2), 024004.
44. Shin, D.; Saparov, B.; Mitzi, D. B., Defect Engineering in Multinary Earth-Abundant Chalcogenide Photovoltaic Materials. *Advanced Energy Materials* **2017,** *7* (11), 1602366.
45. Shin, D.; Zhu, T.; Huang, X.; Gunawan, O.; Blum, V.; Mitzi, D. B., Earth-Abundant Chalcogenide Photovoltaic Devices with over 5% Efficiency Based on a $Cu_2BaSn(S,Se)_4$ Absorber. *Advanced Materials* **2017,** *29* (24), 1606945.
46. Shin, D.; Ngaboyamahina, E.; Zhou, Y.; Glass, J. T.; Mitzi, D. B., Synthesis and Characterization of an Earth-Abundant $Cu_2BaSn(S,Se)_4$ Chalcogenide for Photoelectrochemical Cell Application. *The Journal of Physical Chemistry Letters* **2016,** *7* (22), 4554-4561.
47. Zhou, Y.; Shin, D.; Ngaboyamahina, E.; Han, Q.; Parker, C. B.; Mitzi, D. B.; Glass, J. T., Efficient and Stable $Pt/TiO_2/CdS/Cu_2BaSn(S,Se)_4$ Photocathode for Water Electrolysis Applications. *ACS Energy Letters* **2018,** *3* (1), 177-183.
48. Teymur, B.; Zhou, Y.; Ngaboyamahina, E.; Glass, J. T.; Mitzi, D. B., Solution-Processed Earth-Abundant $Cu_2BaSn(S,Se)_4$ Solar Absorber Using a Low-Toxicity Solvent. *Chemistry of Materials* **2018,** *30* (17), 6116-6123.
49. Kuo, J. J.; Aydemir, U.; Pöhls, J.-H.; Zhou, F.; Yu, G.; Faghaninia, A.; Ricci, F.; White, M. A.; Rignanese, G.-M.; Hautier, G.; Jain, A.; Snyder, G. J., Origins of ultralow thermal conductivity in 1-2-1-4 quaternary selenides. *Journal of Materials Chemistry A* **2019,** *7* (6), 2589-2596.
50. Li, Y.; Li, Z.; Zhang, C.; Yang, D.; Liu, T.; Yan, Y.; Liu, W.; Tan, G.; Su, X.; Uher, C.; Tang, X., Ultralow thermal conductivity of $BaAg_2SnSe_4$ and the effect of doping by Ga and In. *Materials Today Physics* **2019,** *9*, 100098.
51. Zhu, T.; Huhn, W. P.; Wessler, G. C.; Shin, D.; Saparov, B.; Mitzi, D. B.; Blum, V., I_2–II–IV–VI_4 (I = Cu, Ag; II = Sr, Ba; IV = Ge, Sn; VI = S, Se): Chalcogenides for Thin-Film Photovoltaics. *Chemistry of Materials* **2017,** *29* (18), 7868-7879.
52. Kim, Y.; Mitzi, D. B., Growth and Photovoltaic Device Application of Cu2BaGe1–xSnxSe4 Films Prepared by Selenization of Sequentially Deposited Precursors. *ACS Applied Energy Materials* **2021,** *4* (10), 11528-11536.
53. Kim, Y.; Hempel, H.; Unold, T.; Mitzi, D. B., Ag Alloying in $Cu_{2-y}Ag_yBa(Ge,Sn)Se_4$ Films and Photovoltaic Devices. **2023,** *7*, 2201058.
54. Shin, D.; Saparov, B.; Zhu, T.; Huhn, W. P.; Blum, V.; Mitzi, D. B., $BaCu_2Sn(S,Se)_4$: Earth-Abundant Chalcogenides for Thin-Film Photovoltaics. *Chemistry of Materials* **2016,** *28* (13), 4771-4780.
55. Hong, F.; Lin, W.; Meng, W.; Yan, Y., Trigonal Cu_2-II-Sn-VI_4 (II = Ba, Sr and VI = S, Se) quaternary compounds for earth-abundant photovoltaics. *Physical Chemistry Chemical Physics* **2016,** *18* (6), 4828-4834.
56. Sun, J.-P.; McKeown Wessler, G. C.; Wang, T.; Zhu, T.; Blum, V.; Mitzi, D. B., Structural Tolerance Factor Approach to Defect-Resistant I_2-II-IV-X_4 Semiconductor Design. *Chemistry of Materials* **2020,** *32* (4), 1636-1649.
57. Shannon, R. D., Revised effective ionic radii and systematic studies of interatomic distances in halides and chalcogenides. *Acta Crystallographica Section A* **1976,** *32* (5), 751-767.
58. Aitken, J. A.; Larson, P.; Mahanti, S. D.; Kanatzidis, M. G., Li_2PbGeS_4 and Li_2EuGeS_4: Polar chalcopyrites with a severe tetragonal compression. *Chemistry of Materials* **2001,** *13*, 4714-4721.

59. Haferkorn, B.; Meyer, G., Li_2EuSiO_4, ein Europium(II)-dilithosilicat: Eu[$(Li_2Si)O_4$]. *Zeitschrift für anorganische und allgemeine Chemie* **1998,** *624* (7), 1079-1081.
60. Sun, Z.-D.; Chi, Y.; Guo, S.-P., Cu_2EuMQ_4 (M = Si, Ge; Q = S, Se): Syntheses, structure study and physical properties determination. *Journal of Solid State Chemistry* **2019,** *269*, 225-232.
61. Llanos, J.; Mujica, C.; Sánchez, V. c.; Peña, O., Physical and optical properties of the quaternary sulfides $SrCu_2MS_4$ and $EuCu_2MS_4$ (M=Ge and Sn). *Journal of Solid State Chemistry* **2003,** *173* (1), 78-82.
62. Perdew, J. P.; Ernzerhof, M.; Burke, K., Rationale for mixing exact exchange with density functional approximations. *The Journal of Chemical Physics* **1996,** *105* (22), 9982-9985.
63. Heyd, J.; Scuseria, G. E.; Ernzerhof, M., Hybrid functionals based on a screened Coulomb potential. *The Journal of Chemical Physics* **2003,** *118* (18), 8207-8215.
64. Krukau, A. V.; Vydrov, O. A.; Izmaylov, A. F.; Scuseria, G. E., Influence of the exchange screening parameter on the performance of screened hybrid functionals. *The Journal of Chemical Physics* **2006,** *125* (22).
65. Heyd, J.; Scuseria, G. E.; Ernzerhof, M., Erratum: "Hybrid functionals based on a screened Coulomb potential" [J. Chem. Phys. 118, 8207 (2003)]. *The Journal of Chemical Physics* **2006,** *124* (21), 219906.
66. Onida, G.; Reining, L.; Rubio, A., Electronic excitations: density-functional versus many-body Green's-function approaches. *Reviews of Modern Physics* **2002,** *74* (2), 601-659.
67. Mori-Sánchez, P.; Cohen, A. J.; Yang, W., Localization and Delocalization Errors in Density Functional Theory and Implications for Band-Gap Prediction. *Physical Review Letters* **2008,** *100* (14), 146401.
68. Rangel, T.; Del Ben, M.; Varsano, D.; Antonius, G.; Bruneval, F.; da Jornada, F. H.; van Setten, M. J.; Orhan, O. K.; O'Regan, D. D.; Canning, A.; Ferretti, A.; Marini, A.; Rignanese, G.-M.; Deslippe, J.; Louie, S. G.; Neaton, J. B., Reproducibility in G_0W_0 calculations for solids. *Computer Physics Communications* **2020,** *255*, 107242.
69. Ren, X.; Merz, F.; Jiang, H.; Yao, Y.; Rampp, M.; Lederer, H.; Blum, V.; Scheffler, M., All-electron periodic G_0W_0 implementation with numerical atomic orbital basis functions: Algorithm and benchmarks. *Physical Review Materials* **2021,** *5* (1), 013807.
70. Kim, S.; Lee, M.; Hong, C.; Yoon, Y.; An, H.; Lee, D.; Jeong, W.; Yoo, D.; Kang, Y.; Youn, Y.; Han, S., A band-gap database for semiconducting inorganic materials calculated with hybrid functional. *Scientific Data* **2020,** *7* (1), 387.
71. Paier, J.; Asahi, R.; Nagoya, A.; Kresse, G., Cu_2ZnSnS_4 as a potential photovoltaic material: A hybrid Hartree-Fock density functional theory study. *Physical Review B* **2009,** *79* (11), 115126.
72. Skone, J. H.; Govoni, M.; Galli, G., Nonempirical range-separated hybrid functionals for solids and molecules. *Physical Review B* **2016,** *93* (23), 235106.
73. Deák, P.; Aradi, B.; Frauenheim, T.; Janzén, E.; Gali, A., Accurate defect levels obtained from the HSE06 range-separated hybrid functional. *Physical Review B* **2010,** *81* (15), 153203.
74. Blum, V.; Gehrke, R.; Hanke, F.; Havu, P.; Havu, V.; Ren, X.; Reuter, K.; Scheffler, M., Ab initio molecular simulations with numeric atom-centered orbitals. *Computer Physics Communications* **2009,** *180* (11), 2175-2196.
75. Ren, X.; Rinke, P.; Blum, V.; Wieferink, J.; Tkatchenko, A.; Sanfilippo, A.; Reuter, K.; Scheffler, M., Resolution-of-identity approach to Hartree–Fock, hybrid density functionals, RPA, MP2 and GW with numeric atom-centered orbital basis functions. *New Journal of Physics* **2012,** *14* (5), 053020.
76. Havu, V.; Blum, V.; Havu, P.; Scheffler, M., Efficient O(N) integration for all-electron electronic structure calculation using numeric basis functions. *Journal of Computational Physics* **2009,** *228* (22), 8367-8379.
77. Knuth, F.; Carbogno, C.; Atalla, V.; Blum, V.; Scheffler, M., All-electron formalism for total energy strain derivatives and stress tensor components for numeric atom-centered orbitals. *Computer Physics Communications* **2015,** *190*, 33-50.

78. Huhn, W. P.; Blum, V., One-hundred-three compound band-structure benchmark of post-self-consistent spin-orbit coupling treatments in density functional theory. *Physical Review Materials* **2017,** *1* (3), 033803.
79. Jensen, S. R.; Saha, S.; Flores-Livas, J. A.; Huhn, W.; Blum, V.; Goedecker, S.; Frediani, L., The Elephant in the Room of Density Functional Theory Calculations. *The Journal of Physical Chemistry Letters* **2017,** *8* (7), 1449-1457.
80. Lejaeghere, K.; Bihlmayer, G.; Björkman, T.; Blaha, P.; Blügel, S.; Blum, V.; Caliste, D.; Castelli, I. E.; Clark, S. J.; Dal Corso, A.; de Gironcoli, S.; Deutsch, T.; Dewhurst, J. K.; Di Marco, I.; Draxl, C.; Dułak, M.; Eriksson, O.; Flores-Livas, J. A.; Garrity, K. F.; Genovese, L.; Giannozzi, P.; Giantomassi, M.; Goedecker, S.; Gonze, X.; Grånäs, O.; Gross, E. K. U.; Gulans, A.; Gygi, F.; Hamann, D. R.; Hasnip, P. J.; Holzwarth, N. A. W.; Iuşan, D.; Jochym, D. B.; Jollet, F.; Jones, D.; Kresse, G.; Koepernik, K.; Küçükbenli, E.; Kvashnin, Y. O.; Locht, I. L. M.; Lubeck, S.; Marsman, M.; Marzari, N.; Nitzsche, U.; Nordström, L.; Ozaki, T.; Paulatto, L.; Pickard, C. J.; Poelmans, W.; Probert, M. I. J.; Refson, K.; Richter, M.; Rignanese, G.-M.; Saha, S.; Scheffler, M.; Schlipf, M.; Schwarz, K.; Sharma, S.; Tavazza, F.; Thunström, P.; Tkatchenko, A.; Torrent, M.; Vanderbilt, D.; van Setten, M. J.; Van Speybroeck, V.; Wills, J. M.; Yates, J. R.; Zhang, G.-X.; Cottenier, S., Reproducibility in density functional theory calculations of solids. *Science* **2016,** *351* (6280), aad3000.
81. Levchenko, S. V.; Ren, X.; Wieferink, J.; Johanni, R.; Rinke, P.; Blum, V.; Scheffler, M., Hybrid functionals for large periodic systems in an all-electron, numeric atom-centered basis framework. *Computer Physics Communications* **2015,** *192*, 60-69.
82. Ihrig, A. C.; Wieferink, J.; Zhang, I. Y.; Ropo, M.; Ren, X.; Rinke, P.; Scheffler, M.; Blum, V., Accurate localized resolution of identity approach for linear-scaling hybrid density functionals and for many-body perturbation theory. *New Journal of Physics* **2015,** *17* (9), 093020.
83. McKeown Wessler, G. C.; Wang, T.; Sun, J.-P.; Liao, Y.; Fischer, M. C.; Blum, V.; Mitzi, D. B., Structural, Optical, and Electronic Properties of Two Quaternary Chalcogenide Semiconductors: Ag_2SrSiS_4 and Ag_2SrGeS_4. *Inorganic Chemistry* **2021,** *60* (16), 12206-12217.
84. Chang, E. T.; Koknat, G.; Wessler, G. C. M.; Yao, Y.; Blum, V.; Mitzi, D. B., Phase Stability, Band Gap Tuning, and Rashba Splitting in Selenium-Alloyed Bournonite: $CuPbSb(S_{1-x}Se_x)_3$. *Chemistry of Materials* **2023,** *35* (2), 595-608.
85. McKeown Wessler, G. C.; Wang, T.; Blum, V.; Mitzi, D. B., Cubic Crystal Structure Formation and Optical Properties within the Ag–BII–MIV–X (BII = Sr, Pb; MIV = Si, Ge, Sn; X = S, Se) Family of Semiconductors. *Inorganic Chemistry* **2022,** *61* (6), 2929-2944.
86. Wessler, G. C.; Zhu, T.; Sun, J.-P.; Harrell, A.; Huhn, W. P.; Blum, V.; Mitzi, D. B., Band Gap Tailoring and Structure-Composition Relationship within the Alloyed Semiconductor $Cu_2BaGe_{1-x}Sn_xSe_4$. *Chemistry of Materials* **2018,** *30* (18), 6566-6574.
87. Perdew, J. P.; Burke, K.; Ernzerhof, M., Generalized Gradient Approximation Made Simple. *Physical Review Letters* **1996,** *77* (18), 3865-3868.
88. MacDonald, A. H.; Vosko, S. H.; Coleridge, P. T., Extensions of the tetrahedron method for evaluating spectral properties of solids. *Journal of Physics C: Solid State Physics* **1979,** *12* (15), 2991.
89. Von Kubelka, P., Ein Beitrag zur Optik der Farbanstriche. *Zeitschrift fur technische Physik* **1931**, 593-601.
90. Bergerhoff, G.; Brown, I. D.; F.H., A., Crystallographic Databases. **1987**.
91. Wu, K.; Zhang, B.; Yang, Z.; Pan, S., New Compressed Chalcopyrite-like $Li_2BaMIVQ_4$ (MIV = Ge, Sn; Q = S, Se): Promising Infrared Nonlinear Optical Materials. *Journal of the American Chemical Society* **2017,** *139* (42), 14885-14888.
92. Jiang, H.; Gomez-Abal, R. I.; Rinke, P.; Scheffler, M., Localized and Itinerant States in Lanthanide Oxides United by GW@LDA+U. *Physical Review Letters* **2009,** *102* (12), 126403.
93. Johansson, B.; Abrikosov, I. A.; Aldén, M.; Ruban, A. V.; Skriver, H. L., Calculated Phase Diagram for the gamma↔alpha Transition in Ce. *Physical Review Letters* **1995,** *74* (12), 2335-2338.
94. Savrasov, S. Y.; Kotliar, G.; Abrahams, E., Correlated electrons in δ-plutonium within a dynamical mean-field picture. *Nature* **2001,** *410* (6830), 793-795.

95. Piccinin, S., The band structure and optical absorption of hematite (α-Fe2O3): a first-principles GW-BSE study. *Physical Chemistry Chemical Physics* **2019,** *21* (6), 2957-2967.
96. Fedorov, A. V.; Poelchen, G.; Eremeev, S. V.; Schulz, S.; Generalov, A.; Polley, C.; Laubschat, C.; Kliemt, K.; Kaya, N.; Krellner, C.; Chulkov, E. V.; Kummer, K.; Usachov, D. Y.; Ernst, A.; Vyalikh, D. V., Insight into the Temperature Evolution of Electronic Structure and Mechanism of Exchange Interaction in EuS. *The Journal of Physical Chemistry Letters* **2021,** *12* (34), 8328-8334.
97. Bachmann, R.; Wachter, P., Photoconductivity of EuS and EuSe. *Physics Letters A* **1968,** *26* (10), 478-479.
98. Aitken, J. A.; Lekse, J. W.; Yao, J.-L.; Quinones, R., Synthesis, structure and physicochemical characterization of a noncentrosymmetric, quaternary thiostannate: $EuCu_2SnS_4$. *Journal of Solid State Chemistry* **2009,** *182* (1), 141-146.
99. Kim, Y.; Hempel, H.; Levcenco, S.; Euvrard, J.; Bergmann, E.; Gunawan, O.; Unold, T.; Hill, I. G.; Mitzi, D. B., Optoelectronic property comparison for isostructural $Cu_2BaGeSe_4$ and Cu_2BaSnS_4 solar absorbers. *Journal of Materials Chemistry A* **2021,** *9* (41), 23619-23630.
100. Chen, S.; Gong, X. G.; Walsh, A.; Wei, S.-H., Crystal and electronic band structure of Cu_2ZnSnX_4 (X=S and Se) photovoltaic absorbers: First-principles insights. *Applied Physics Letters* **2009,** *94* (4), 041903.
101. Persson, C., Electronic and optical properties of Cu_2ZnSnS_4 and $Cu_2ZnSnSe_4$. *Journal of Applied Physics* **2010,** *107* (5), 053710.
102. Nakamura, S.; Maeda, T.; Wada, T., Electronic structure of stannite-type $Cu_2ZnSnSe_4$ by first principles calculations. *physica status solidi c* **2009,** *6* (5), 1261-1265.
103. Jing, T.; Dai, Y.; Ma, X.; Wei, W.; Huang, B., Electronic Structure and Photocatalytic Water-Splitting Properties of $Ag_2ZnSn(S_{1-x}Se_x)_4$. *The Journal of Physical Chemistry C* **2015,** *119* (50), 27900-27908.

TOC Graphic:

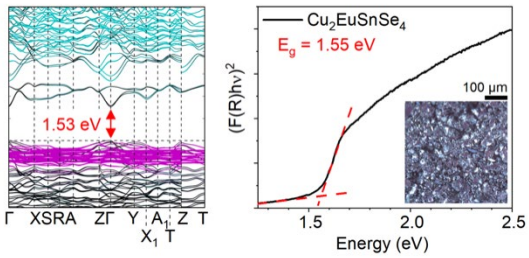
1.53 eV
Γ XSRA ZΓ Y A1 Z T
X1 T
Cu2EuSnSe4
Eg = 1.55 eV
100 μm
(F(R)hν)2
1.5
2.0
2.5
Energy (eV)